

A Parameterized Neutrino Emission Model to Study Mass Ejection in Failed Core-collapse Supernovae

ANDRÉ DA SILVA SCHNEIDER¹ AND EVAN O’CONNOR¹

¹The Oskar Klein Centre, Department of Astronomy, Stockholm University, AlbaNova, SE-106 91 Stockholm, Sweden

(Dated: October 3, 2022)

Submitted to ApJ

ABSTRACT

Some massive stars end their lives as *failed* core-collapse supernovae (CCSNe) and become black holes (BHs). Although in this class of phenomena the stalled supernova shock is not revived, the outer stellar envelope can still be partially ejected. This occurs because the hydrodynamic equilibrium of the star is disrupted by the gravitational mass loss of the protoneutron star (PNS) due to neutrino emission. We develop a simple parameterized model that emulates PNS evolution and its neutrino emission and use it to simulate failed CCSNe in spherical symmetry for a wide range of progenitor stars. Our model allows us to study mass ejection of failed CCSNe where the PNS collapses into a BH within ~ 100 ms and up to $\sim 10^6$ s. We perform failed CCSNe simulations for 262 different pre-SN progenitors and determine how the energy and mass of the ejecta depend on progenitor properties and the equation of state (EOS) of dense matter. In the case of a future failed CCSN observation, the trends obtained in our simulations can be used to place constraints on the pre-SN progenitor characteristics, the EOS, and on PNS properties at BH formation time.

Keywords: Compact objects (288), Hydrodynamics (1963), Neutron stars (1108), Core-collapse supernovae (304), Nuclear astrophysics (1129), Black holes (162)

1. INTRODUCTION

Massive stars with zero-age main-sequence (ZAMS) mass $M_{\text{ZAMS}} \gtrsim 8 M_{\odot}$ undergo a core-collapse event once their nuclear fuel is exhausted. As the inert iron-core collapses onto itself, its density and pressure increase by orders of magnitude within a fraction of a second. This occurs until densities reach nuclear saturation density, $\rho_{\text{sat}} \simeq 2.7 \times 10^{14} \text{ g cm}^{-3}$, and collapse is suddenly halted by the stiffening of nuclear interactions. At this moment, a protoneutron star (PNS) is born where once was the iron core of the massive star. Meanwhile, continuously infalling matter hits the hard PNS and rebounds, creating a shock wave that propagates outwards through the still accreting outer layers of the star. Eventually this shock stalls, due to photodissociation of heavy nuclei and neutrino emission losses, and starts to recede. As matter continues to accrete onto the PNS, neutrino emission increases. If neutrinos leaving the PNS deposit enough energy behind the stalled shock, the shock is revived, unbinding most of the outer layers of the star

and igniting a bright *successful* core-collapse supernova (CCSN).

However, a still unknown fraction of massive stars are expected to undergo a *failed* CCSN event, *i.e.*, the shock wave is not revived and recedes as matter continues to accrete onto the PNS. Once enough matter is accreted, the PNS overcomes the maximum mass it can support and collapses into a black hole (BH) without a bright transient. This BH formation channel could occur for some massive stars and determining the landscape of which massive stars lead to successful explosions and which ones do not is an active topic of research (Sukhbold et al. 2016; Couch et al. 2020; Burrows et al. 2020; Baccioli et al. 2022b). Despite BH formation, mass ejection is still possible for failed SNe because of the hydrodynamic consequences of the neutrino emission that carries away $\mathcal{O}(10\%)$ of the gravitational mass of the PNS. Although these neutrinos barely interact with the outer regions of the star as they fly by, their emission decreases the gravitational pull of the PNS on the outer layers of the collapsing star. The sudden disruption of the hydrostatic equilibrium creates a pressure wave deep within the star that travels outwards, gaining or losing momentum depending on local stellar properties. If the pulse gains enough

momentum it eventually forms a shock that becomes unbound and escapes to the interstellar medium (Nadyozhin 1980; Lovegrove & Woosley 2013; Fernández et al. 2018). In such a BH formation channel, the progenitor star would become momentarily brighter, for a few seconds up to a few days, before dimming significantly or even disappear altogether. Furthermore, ejection of the outer stellar envelope could lead to a bright transient, even if it is orders of magnitude less luminous than typical successful SN. Although a failed SN has never been directly observed, there is some evidence that they do occur (Gerke et al. 2015; Adams et al. 2017; Allan et al. 2020; Murguía-Berthier et al. 2020; Basinger et al. 2021; Neustadt et al. 2021; Rodríguez 2022). However, interpretation of the supposed failed SNe transients and their progenitors is not without controversy and continuing observations are needed to settle the debate (Murphy et al. 2018; Humphreys 2019; Burke et al. 2020; Bear et al. 2022).

Historically, SN surveys seek for the sudden appearance of new light sources in the sky. However, to discover failed SNe one has to look for the opposite effect: a suddenly “disappearing” source. Such survey was proposed by Kochanek et al. (2008) noticing that within a distance of 10 Mpc there are $\simeq 10^6$ red supergiants (RSGs) and that these stars undergo a core-collapse event within $\simeq 10^6$ yr. Thus, within a few years observing stars within 10 Mpc, a survey would be likely to identify one or even a few stars that end their lives either *with a bang (supernova) or a whimper (fall out of sight)* (Kochanek et al. 2008). More recently, Tsuna (2021) proposed a survey to search for soft x-ray emission from collisions of the relatively slow, $\sim 600 - 800 \text{ km s}^{-1}$, and low-mass, $\sim 0.1 M_\odot$, ejecta of failed CCSNe from blue supergiant stars (BSG) in the Large Magellanic Cloud (LMC) with the circumstellar medium (CSM). Even though the expected rate of BSG failed SNe in the LMC is of order 10^{-4} year, these sources are expected to emit detectable x-rays for 10^3 to 10^4 years, depending on mass loss rate before core collapse for typical BSG ejecta (Tsuna 2021). The identification of these CCSN progenitors and determination of their outcome would place new constraints on the rate of core-collapse events as well as the branching ratio of failed SNe. To date, the failed SN rate has been estimated by Neustadt et al. (2021) to be $f = 0.16^{+0.23}_{-0.12}$ of all CCSNe and by Byrne & Fraser (2022) to be $f < 0.23$ for sources with absolute magnitude < -14 .

Another reason to identify CCSNe progenitors, especially of failed CCSNe, is to shed light on the “red supergiant problem”. SN surveys by Smartt et al. (2009) and Williams et al. (2014) have shown that RSGs that are SN progenitors seem to be limited to $M_{\text{ZAMS}} \lesssim 16.5 M_\odot$ and $M_{\text{ZAMS}} \lesssim 20 M_\odot$, respectively, while some RSGs have $M_{\text{ZAMS}} \simeq 25 M_\odot$. A possible solution to this problem is that stars in the range $17 - 20 M_\odot \lesssim M_{\text{ZAMS}} \lesssim 25 M_\odot$ undergo failed CCSN events. However, detection selec-

tion effects or distinct stellar evolution pathways for stars in the $17 - 20 M_\odot \lesssim M_{\text{ZAMS}} \lesssim 25 M_\odot$ range could account for the discrepancy (Kochanek et al. 2008; Smartt et al. 2009; Bear et al. 2022). Therefore, unambiguous determination of a failed SN from a RSG progenitor could settle the debate around the RSG problem.

While direct observations are lacking, theoretical and computational works are necessary to evaluate the possible signatures of failed SN and to unequivocally match them to surveys. Analytic estimates by Piro (2013) show that the response of a RSG to the sudden loss of a few $0.1 M_\odot$ in gravitational mass by the PNS is a shock breakout with luminosity $\sim 10^{40} - 10^{41} \text{ erg s}^{-1}$ that lasts $\sim 3 - 10$ days. Lovegrove & Woosley (2013), also studying RSG models, demonstrated that failed CCSNe are capable of unbinding the hydrogen envelope of RSGs; leading to faint, red, long-duration observable transients with luminosity $\sim 10^{39} \text{ erg s}^{-1}$ that lasts approximately a year. A main difference between the timescales of the events as predicted by Piro (2013) and Lovegrove & Woosley (2013) is that in the former the transient is powered by the kinetic energy of the ejected mass while in the latter the ejected envelope emits its energy via hydrogen recombination. Numerical simulations by Lovegrove et al. (2017) of the light curve and spectra of failed CCSNe from two RSG progenitors with $M_{\text{ZAMS}} = 15 M_\odot$ and $25 M_\odot$ considering a range of explosion energies show that the peak bolometric luminosity can be in the range $\sim 10^{39} - 10^{44} \text{ erg s}^{-1}$ depending on explosion energy, which is a function of the equation of state (EOS) and the pre-SN progenitor core compactness, structure, and mass. An increase in the maximum mass supported by the PNSs before BH collapse, which is expected if the EOS of dense matter is stiff, results in a net increase of neutrino emission and a stronger shock. Also discussed by Lovegrove et al. (2017) is the importance of accurately modeling stellar atmosphere, opacity, and ambient medium to determine the observational prospects of failed SN with current and forthcoming missions.

The failed CCSN mass ejection mechanism has also been analyzed analytically by Coughlin et al. (2018) using linear perturbation theory. Their predictions for the stellar response to the sudden loss of gravitational mass in the core agree well with spherically-symmetric simulation results of Fernández et al. (2018); Ivanov & Fernández (2021), respectively, F18 and I21 from now on. While F18 used a parametric prescription to approximate the PNS neutrino mass loss using the non-relativistic FLASH code (Fryxell et al. 2000; Dubey et al. 2009), I21 performed detailed numerical simulations of the PNS evolution up to BH formation using the general-relativistic GR1D code (O’Connor 2015) and mapped the result to FLASH to gauge the ejecta properties. Both works showed that mass ejection in failed CCSNe is sensitive to pre-SN progenitor structure, the dense-matter EOS, and, to a smaller degree, to the timescale of grav-

itational mass loss by neutrino emission, and, might not occur at all for some progenitors.

In this work we perform simplified numerical simulations of failed CCSNe. First, we develop a model to estimate neutrino emission and BH formation times for CCSNe based on spherically-symmetric simulations using FLASH (Fryxell et al. 2000; Dubey et al. 2009; Couch 2013; O’Connor & Couch 2018) and M1 neutrino transport (O’Connor 2015). Extending the simulations of Schneider et al. (2020) (S20 henceforth) to a few other progenitors, we show that (1) the evolution of the neutrino luminosity can be well fitted by a function of the accretion rate onto the PNS and its baryonic mass and that (2) the entropy inside the PNS, which determines BH formation for an EOS, is well approximated by a function of the mass of the PNS and the time since the PNS has formed. Together, these two approximations allow us to simulate failed CCSNe by replacing the PNS and BH physics by a simple model that includes accretion of the supersonically infalling outer layers of the star and the loss of gravitational mass due to neutrino emission without having to solve computationally expensive neutrino transport equations.

Employing our model for PNS neutrino emission and BH formation we perform CCSNe simulations in spherical symmetry for a wide range of pre-SN progenitor stars found in the literature. We watch as a sound pulse forms in the outer layers of the star due to the loss in core gravitational mass and run our simulations well past BH formation until the sound pulse either becomes a shock and unbinds from the star or falls back into the BH. By using a large set of simulations we determine the dependence of the mass ejecta and its energy as a function of the pre-SN progenitor properties and EOS.

We discuss our model of neutrino emission and PNS evolution during CCSNe in Section 2. To validate our model, in Section 3 we compare PNS evolution until BH formation using our template to results obtained with significantly more computationally expensive core-collapse simulations that use M1 neutrino transport. In Section 4 we use our parameterized model to predict the impact of progenitor structure and EOS on the properties of failed CCSNe. We conclude in Section 5.

2. MODEL

We first review the main result of S20 and, then, use the insights gained to parameterize the PNS entropy evolution and its neutrino emission.

2.1. Black hole formation

In S20 we have shown that for a given pre-SN progenitor the PNS gravitational mass and its *most common entropy*¹, simply referred to as entropy from now on,

¹ The *most common entropy* \bar{s} is defined as the value of the approximately flat PNS entropy that contains the largest amount of mass.

evolve almost independently of the EOS up to the point of BH formation. However, the BH formation time and the EOS of dense matter. The latter was hinted at by Hempel et al. (2012); Steiner et al. (2013) discussing the core collapse of a single progenitor star and many EOSs.

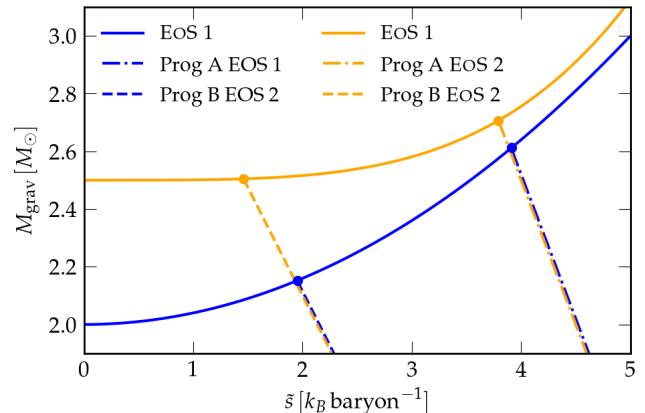


Figure 1. PNS mass-entropy evolution scheme up to the point of BH formation for two different EOSs and two pre-SN progenitor stars. Tracks for high-compactness progenitor A (dash-dotted lines) and low-compactness progenitor B (dashed lines) start at low M_{grav} and move to higher mass and lower entropy as matter is accreted and neutrinos are emitted. The PNS collapses into a BH earlier (lower PNS mass) for the softer EOS 1 than the stiffer EOS 2.

For clarity and simplicity we show in Figure 1 a scheme with four PNS mass-entropy evolution tracks for the core collapse of two different pre-SN progenitor stars, each one evolved considering two different dense-matter EOSs. In the scheme, dashed and dot-dashed tracks show the entropy evolution of the PNS as a function of the PNS gravitational mass up to the point of BH formation. The latter depends on the maximum mass supported by a PNS at finite entropy, shown as solid lines in the plot. In the plot, progenitor A is a massive star with a compactness larger than that of progenitor B. Hence, as the iron core of progenitor A collapses it forms a PNS that accretes matter faster than the PNS formed by the core collapse of progenitor B. Faster accretion leads to higher energy deposition onto the PNS and, thus, higher temperatures and entropies inside the PNS. This explains why progenitor A has a higher entropy than progenitor B for the same PNS mass. Nevertheless, the entropy of both PNSs decrease as they become more massive, as entropy is carried away by neutrino emission. In the case of pre-SN progenitors with mass-entropy tracks similar to those of progenitor A, due to fast accretion of matter, not much time elapses before the mass of the PNS overcomes the maximum mass that can be supported by the PNS at a given entropy and a BH forms. For entropies of the magnitudes shown for progenitor A, the time from core bounce to BH forma-

tion is $t_{\text{BH}} - t_{\text{bounce}} \lesssim 0.5$ s. Meanwhile, PNSs formed in CCSNe that have similar $M_{\text{grav}} - \tilde{s}$ tracks to progenitor B accrete matter slower due to the lower accretion rates onto the PNS and $t_{\text{BH}} - t_{\text{bounce}} \gtrsim 1$ s.

As shown in Figure 1, the PNS mass-entropy evolution for a given progenitor does not depend significantly on the EOS up to the point of BH formation, shown by filled circles in the scheme. The moment the BH forms, however, is EOS dependent. In Figure 1 we compare two different EOSs: EoS 1 is a softer EOS than EoS 2 at lower temperatures (low entropy), while both EOSs have similar stiffness at higher temperatures (high entropy). Therefore, for the more (less) compact progenitor A (B) the difference in PNS gravitational mass at the moment of BH formation is relatively small (large), $\simeq 0.1 M_{\odot}$ ($\simeq 0.4 M_{\odot}$). Although there are only a few constraints on the maximum mass supported by a PNS at a given entropy, most models predict a maximum supported mass that increases with entropy (Schneider et al. 2020; Steiner et al. 2013).

The picture outlined above highlights that it would be difficult to extrapolate zero temperature NS properties from the observation of the formation of a BH from a CCSN. Nevertheless, this picture is useful to simplify the study of failed CCSNe since we are able to create a template for neutrino luminosity and PNS entropy evolution from the outcome of only a few simulations. With a reasonable template we are able to determine time dependent neutrino emission from a PNS as well as the BH formation time for different progenitors and EOSs without having to solve computationally expensive neutrino transport equations. We discuss this now.

2.2. Protoneutron star entropy model

To create a simple template for PNS entropy evolution we perform spherically symmetric simulations of CCSNe using the FLASH-code (Fryxell et al. 2000; Dubey et al. 2009; Couch 2013; O’Connor & Couch 2018). Our simulations employ the SRO baseline EOS of Schneider et al. (2019b); Eggenberger Andersen et al. (2021) and the neutrino transport library NuLIB of O’Connor (2015) as discussed in detail in S20, Section 2.3.

We simulate the core collapse of many pre-SN progenitors with core-compactness $\xi_{2.5}$ spanning the range $\sim 10^{-4.5}$ to ~ 1 and envelope compactness ξ_{env} in the range ~ 0.01 to ~ 30 . Core-compactness is defined as in O’Connor & Ott (2011),

$$\xi_M = \frac{M/M_{\odot}}{R(M_{\text{baryon}} = M)/1000 \text{ km}} \Big|_{t=t_{\text{cc}}}, \quad (1)$$

and envelope compactness as in F18,

$$\xi_{\text{env}} = \frac{M_{\text{cc}}/M_{\odot}}{R_{\text{cc}}/R_{\odot}} \Big|_{t=t_{\text{cc}}}, \quad (2)$$

where M_{cc} , R_{cc} , and t_{cc} are the progenitor mass, radius, and time at the start of core collapse. The list of

Table 1. Pre-SN progenitor name, zero age main sequence mass (M_{ZAMS}), total pre-SN mass at the start of core collapse (M_{cc}), iron core mass (M_{Fe}), core-compactness parameters $\xi_{2.5}$ (O’Connor & Ott 2011), envelope compactness ξ_{env} , and metallicity z relative to that of the Sun z_{\odot} , $[z] = \log_{10}(z/z_{\odot})$ where “x” means no metals. Compactness, $\xi_{2.5}$, values are for pre-SN progenitors at the start of collapse and, thus, differ from the ones of O’Connor & Ott (2011), which were computed for a single EOS at the moment of core bounce.

Name	M_{ZAMS} [M_{\odot}]	M_{cc} [M_{\odot}]	M_{Fe} [M_{\odot}]	$\xi_{2.5}$	ξ_{env}	[z]
Fernández et al. (2018) ^a						
R12z00	12.0	10.0	1.45	0.151	0.009	0.
W26z00	26.0	11.9	1.59	0.214	10.8	0.
Y25z-2	25.0	23.0	1.62	0.256	0.024	-2.
W40z00	40.0	10.3	1.78	0.370	27.1	0.
R15z00	15.0	10.8	1.50	0.239	0.010	0.
B25z00	25.0	11.7	1.60	0.336	0.12	0.
B30z-2	30.0	16.0	1.72	0.337	0.11	-2.
Y22z00	22.0	11.1	1.85	0.546	0.016	0.
W50z00	50.0	9.2	1.91	0.554	21.9	0.
B80z-2	80.0	55.2	3.32	0.972	0.79	-2.
Woosley & Heger (2007)						
s50	50.0	9.76	1.50	0.216	30.1	0.
s25	25.0	15.8	1.60	0.326	0.011	0.
s40	40.0	15.3	1.83	0.534	1.40	0.
Woosley et al. (2002)						
z11	11.0	11.0	1.25	0.005	0.591	x
z12	12.0	12.0	1.36	0.011	0.997	x
z13	13.0	13.0	1.45	0.025	1.255	x
z14	14.0	14.0	1.40	0.041	1.354	x
z25	25.0	25.0	1.81	0.385	2.148	x
u40	40.0	40.0	1.90	0.633	0.457	-4
u75	75.0	74.1	2.03	0.873	0.299	-4
Limongi & Chieffi (2006) (LC06A)						
s60	60.0	16.9	1.63	0.424	0.081	0.
s80	80.0	22.4	1.67	0.481	0.111	0.
s120	120.0	30.5	1.91	0.534	0.143	0.
Sukhbold et al. (2016) [10^{-4}]						
s9.0	9.0	8.75	1.32	0.382	0.021	0.
s10.0	10.0	9.68	1.34	1.99	0.019	0.

^a The MESA (Paxton et al. 2011, 2013, 2015, 2018, 2019) inlists to generate the CCSN progenitors were obtained from https://bitbucket.org/rafernan/bhsn_mesa_progenitors/src/master/.

progenitors used to create a PNS mass-entropy evolution template and their properties are shown in Table 1.

For each simulation we compute the entropy \tilde{s} inside the PNS for 100 equally separated time instants from core bounce until a BH forms or, in the case of low-compactness models, until $t_{\text{simulation}} - t_{\text{cc}} = 10$ s. We then fit the entropy as a function of two variables using a second-order-splines interpolation scheme (Virtanen et al. 2020). The variables are (1) base-10 logarithm of the simulation time after core bounce, $\log_{10} t$ where $t = t_{\text{simulation}} - t_{\text{bounce}}$, and (2) the baryonic mass inside a radius of 500 km, M_{500} . Here $t_{\text{simulation}}$ is the time from the start of the simulation and we approximate the bounce time t_{bounce} as the time after the central density of the star reaches $10^{12} \text{ g cm}^{-3}$.

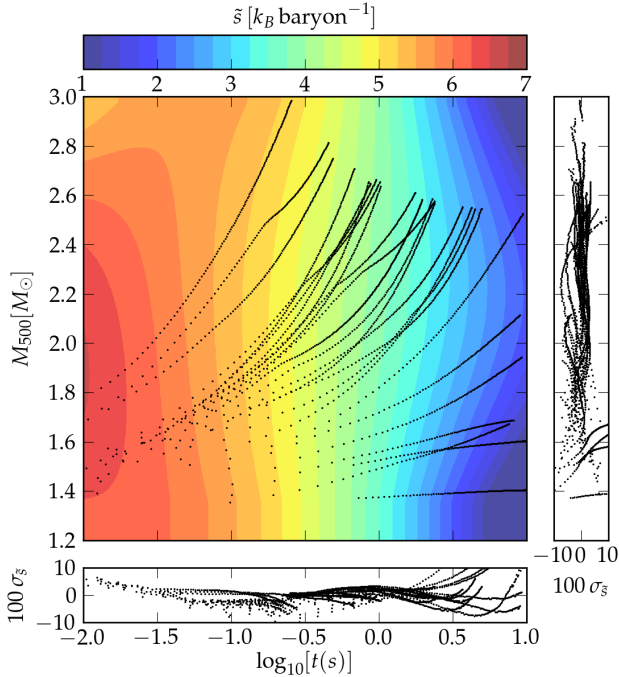


Figure 2. Entropy \tilde{s} fit based on CCSN simulations of the pre-SN progenitors described in Table 1. The values of t and M_{500} used to fit the entropy are shown as black dots in the main plot. The deviations $\sigma_{\tilde{s}}$ between the fit and the entropy computed from the simulations are shown in the bottom and right plots and are usually 5% or better.

In Figure 2, we show the results of the entropy fit $\tilde{s}(t, M_{500})$, the tracks in $t - M_{500}$ space for each core-collapse simulation using the progenitors of Table 1, and the deviations between the fit and the simulation results. First, we observe that in the first second after bounce, the PNS entropy is, to first order, only a function of time after core bounce, *i.e.*, almost independent of progenitor compactness or PNS mass. Thus, for compact progenitors that form BHs in $t \lesssim 1$ s, it would have been sufficient to fit the entropy as a function of time. However, since the trend breaks down for PNSs that take longer than 1 s to collapse into a BH, we opt

for a more robust two variable fit. Note that the fit for massive PNSs when $M_{500} \gtrsim 2.5 M_{\odot}$ and $t \gtrsim 1$ s predicts decreasing entropy with increasing mass. This may be unrealistic and simply an artifact of the fitting as these regions in phase space are not populated by our simulations. We also notice that the deviation in entropy between the fit and the simulations are often within 5% of each other, with the largest deviations taking place near the end of each. Furthermore, changes of $\sim 10\%$ in the estimated PNS entropy do not alter significantly the BH formation time and its initial mass. For very-low compactness progenitors, which take significantly longer than 10 s to form a BH, we expect changes in entropy to cause an even smaller relative error in the BH formation time, as the maximum mass supported by the EOS does not change more than $0.1 M_{\odot}$ compared to that of a cold NS. In Section 2.4 we discuss how we approach neutrino emission for supernova progenitors that take more than 10 s after core bounce to form a BH.

2.3. Neutrino emission model

Similar to what is done for the PNS entropy, we also fit the neutrino luminosity L_{ν} for the three neutrino species considered in our simulations, $\nu = \nu_e, \bar{\nu}_e, \nu_x$ where ν_x includes contributions from $x = \mu, \bar{\mu}, \tau$, and $\bar{\tau}$ neutrino species. The neutrino luminosity fits are done for each neutrino species independently and are interpolated as a function of (1) the mass inside a radius of 500 km from the center of the star, M_{500} , and (2) the accretion rate at 500 km, \dot{M}_{500} , using a radial-basis function interpolation scheme. We chose the variables M_{500} and \dot{M}_{500} , instead of $\log_{10} t$ and M_{500} as in the entropy template, because they provide a considerable better fit to the neutrino luminosity and are similar to the variables used in the analytic neutrino luminosity approximation of Lovegrove & Woosley (2013) and F18.

In Figure 3, we show the electron neutrino luminosity fit, L_{ν_e} , and the path traced in $M_{500} - \dot{M}_{500}$ by the PNSs generated by the collapse of the progenitors described in Table 1. The interpolated luminosity is usually within 20% of the simulated values although large deviations do occur at selected times. Specifically, during the neutronization burst, when the accretion rate is $\mathcal{O}(10 M_{\odot} \text{ s}^{-1})$, and at times where the accretion rate has a sharp decrease due to the accretion of a shell boundary at 500 km. Since such moments are quite brief with respect to the BH formation time, their contributions to the total neutrino luminosity are small. We observe similar trends for the luminosity fits of the other two neutrino species, $\bar{\nu}_e$ and ν_x , except for the lack of a neutronization burst.

Our method to predict neutrino luminosity during CCNSe has other limitations. First, we observe that neutrino luminosity predicted using our simplified model can, in some instances, deviate significantly from the full M1 neutrino-transport scheme calculations. This effect is stronger for the heavy neutrino luminosity L_{ν_x} and is

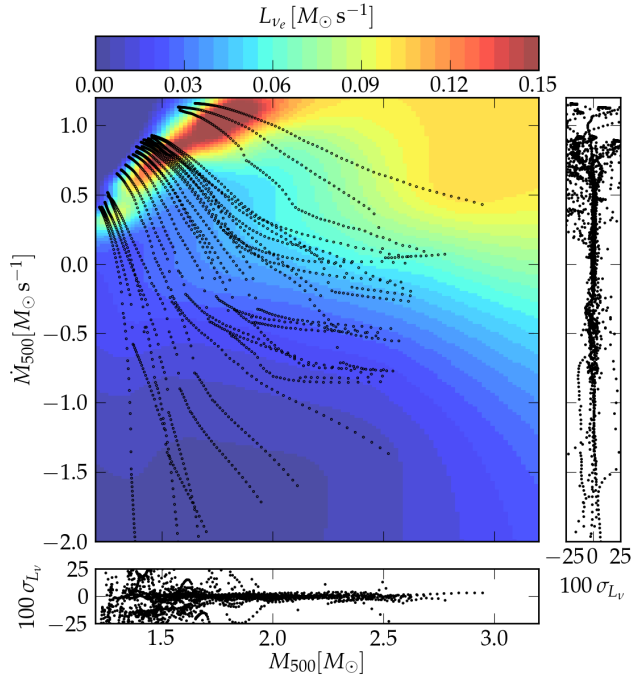


Figure 3. Electron neutrino luminosity L_{ν_e} fit based on simulations of pre-SN progenitors described in Table 1. The values of M_{500} and \dot{M}_{500} used to fit the neutrino luminosity are shown as black dots in the main plot. The deviations $\sigma_{L_{\nu_e}}$ between the fit and the luminosity computed from the simulations are shown in the bottom and right plots. Deviations are usually $\lesssim 15\%$, except for regions in the parameter space where accretion is high or drops very quickly due to accretion of a shell boundary. Note that $0.1 M_{\odot} \simeq 1.8 \times 10^{53}$ erg.

especially true for stiff EOSs, which increase the time to form BHs. This is in part because to simulate core collapse with stiffer EOSs, where BH formation occurs for larger PNS masses, we have to extrapolate the neutrino luminosity fits into regions of the $M_{500} - \dot{M}_{500}$ parameter space that our template, based on results obtained with the SRO baseline EOS, does not cover. We discuss these effects further in Section 3.

Low-compactness progenitors accrete matter very slowly and, therefore, take a long time to collapse into a BH, $t \gtrsim 10$ s after core-bounce. Since our model is limited to fits where $\dot{M}_{500} > 0.01 M_{\odot} s^{-1}$, extrapolation from this region may lead to relatively high neutrino luminosity at late times. In fact, while accretion leads to an increase in baryonic mass, extrapolating from the parameter space probed can result in unrealistically high or low neutrino luminosity, which can lead to BHs forming too fast (no neutrino emission) or never forming at all (neutrino luminosity larger than accretion rate). To prevent this unrealistic scenarios, we cap the neutrino luminosity L_{ν} for each species to $\dot{M}_{500}/10$. This scenario only affects low compact-

ness progenitors several seconds after core bounce, when neutrino emission is expected to dissipate any thermal heat gain due to accretion in time scales much shorter than the accretion timescales. Thus, to a good approximation, we may consider such NSs to be cold, zero temperature, and slowly increasing their mass. We remark that for most EOSs and cold NSs with baryonic mass $M_{\text{baryon}} \gtrsim 1.5 M_{\odot}$, $dE_{\text{bind}}/dM_{\text{baryon}} \sim 0.30 - 0.35$, where $E_{\text{bind}} = M_{\text{baryon}} - M_{\text{grav}}$ is the binding energy of the cold NS. Thus, by capping the neutrino emission rates to a combined luminosity of $\sim 0.3 \dot{M}_{500}$ we obtain a decent estimate of neutrino emission at late times.

2.4. Simulations

The parameterizations discussed above allow us to simulate the outcome of failed CCSNe without having to solve the computationally expensive neutrino transport equations. This, we are able to simulate failed SN from the start of core collapse until shock breakout, if it occurs, which may be minutes to years after BH forms depending on the progenitor star. The simulations are performed using the FLASH4 code (Fryxell et al. 2000; Dubey et al. 2009; Couch 2013; O’Connor & Couch 2018) in spherical symmetry. The code is adapted to estimate the PNS entropy \tilde{s} and neutrino luminosity L_{ν} using the parameterized templates described above. Our runs are divided in three stages discussed below. In every run, we use a spherical grid with adaptive mesh refinement that extends out to 2×10^{12} cm in the first two stages and then mapped onto a grid that extends to 2.048×10^{15} cm in the last stage. In all stages, on the coarsest level, there are 256 grid zones and we allow up to 20 total levels of refinement resulting in a smallest grid zone with a length of 149 m for the first two stages and 153 km for the last stage.

2.4.1. Stage 1: Before core bounce

We evolve the core-collapse of the pre-SN progenitor until the central density reaches $\rho_c = 10^{12} \text{ g cm}^{-3}$. We do not use any neutrino transport and set $t = 0$ (core bounce) at the end of this stage. Simulating this short period before core bounce is necessary to accurately reproduce the mass accretion rate onto the PNS after core bounce, which is crucial to use the neutrino luminosity template discussed in Section 2.3.

2.4.2. Stage 2: From core bounce to BH formation

At core bounce we replace the inner $r = r_0 = 100$ km of the simulation volume by a “hole” with constant density ρ_{hole} . The density ρ_{hole} is computed assuming that the hole contains a mass that is equal to half of the mass between r and $2r$, guaranteeing that $\rho_{\text{hole}} \ll \rho(r_0)$ for $r = r_0$ and, thus, the mass just outside the hole free-falls onto the PNS. This reproduces the expected accretion rate for CCSNe that do not lead to successful explosion, as is the case for all spherically-symmetric simulations

for the pre SN progenitors probed in this work². The “missing” gravitational mass from decreasing the density in the region within the hole radius r is placed as a point mass at the origin. In order to increase the time step of the simulation as the system evolves, the hole size is increased with a constant speed such that $r = r_0 + vt$, where we set $v = 10 \text{ km s}^{-1}$. The point mass at the origin and the hole density are evolved according to the hole size evolution and the neutrino emission computed from our templates.

We estimate the gravitational mass inside the 500 km sphere used in our templates to be $M_{\text{grav}}(t) = M_{500}(t) - E_{\nu}(t)$, where $E_{\nu}(t) = \sum_{\nu} \int_0^t L_{\nu}(t') dt'$ is the total energy emitted in neutrinos and the sum runs over the three neutrino species considered. This approach is justified as, to a very good approximation, neutrinos are the only source of gravitational mass loss. By tracking the entropy and gravitational mass evolution we determine the moment a BH forms from $M_{\text{grav}}(t) = M_{\text{grav}}^{\text{max}}(s(t))$ where $s(t)$ is the template estimate for the PNS entropy. The point of BH formation depends on $M_{\text{grav}}^{\text{max}}(s)$, which can be set to some fixed value or be computed for a desired EOS, see Figure 1. Low-compactness progenitors may take significantly longer than 40 s to collapse into a BH, the time when the hole radius reaches the 500 km used in our templates. When this happens, we simply compute the baryonic mass and accretion rate at the hole radius r instead of 500 km as the time for matter accreted at r to reach 500 km is significantly shorter than the dynamical time scale of the system.

2.4.3. Stage 3: after BH formation

Once a BH forms, the neutrino luminosity is set to zero and the total gravitational mass loss from neutrino emission is $\delta M_{\text{grav}} = E_{\nu}(t_{\text{BH}})$. Because of the change in gravitational mass of the inner core, hydrodynamic equilibrium in the outer layers of the pre-SN progenitor is disturbed (Nadyozhin 1980; Lovegrove & Woosley 2013; Coughlin et al. 2018). This perturbation creates a pressure wave that propagates outwards towards the surface of the star and may result in some mass ejection, even in the case of failed SNe. To determine the mass ejection and its energy, we follow the evolution of the system until the pulse turns into a shock and leaves the star or the pulse velocity becomes negative, indicating the pulse will fall back into the BH. We limit the hole radius to $r_{\text{max}} = 2 \times 10^7 \text{ km}$, at which point we fix $r = r_{\text{max}}$. As in F18; I21 we (1) fill the region outside the star with a constant density ambient medium in hydrostatic equilibrium for numeri-

cal reasons and (2) map pressure, density, and proton fractions from the progenitor to recover the remaining thermodynamic variables using the Helmholtz EOS (Timmes & Swesty 2000) to minimize transients. The ambient medium is set to a hydrogen gas with density $\rho_{\text{amb}} = \{10^{-18}, 10^{-16}, 10^{-14}, 5 \times 10^{-13}\} \text{ g cm}^{-3}$ for stars with radii $R > \{10^8, 10^7, 10^6, 10^5\} \text{ km}$, respectively. To achieve densities below $10^{-10} \text{ g cm}^{-3}$, the Helmholtz EOS as implemented in FLASH is extended to $10^{-20} \text{ g cm}^{-3}$ using a version of the publicly available Timmes & Arnett (1999) EOS code³. Similar to F18; I21, simulations are terminated once the pulse reaches the atmosphere surrounding the star and its temperature drops to within 1% of the EOS table lower limit, $T_{\text{low}} = 10^4 \text{ K}$ or if the pulse leaves the simulation volume. The spatial resolution of our simulations in the outer regions of the star, $r > 10^8 \text{ cm}$, are $\Delta r/r = 4 \times 10^{-3}$, similar to the low resolution runs of I21. We did not perform detailed resolution studies since I21 showed that resolution is a smaller source of uncertainty than changes in the EOS.

3. TEMPLATE ACCURACY

Using the methods described in Section 2, we assess the accuracy of our model in describing the core collapse of the $40 M_{\odot}$ solar metallicity pre-SN progenitor of Woosley & Heger (2007), s40WH07, using a variety of EOSs. Besides the baseline EOS of S20, used to construct our PNS entropy and neutrino emission templates, we explore 21 other EOSs found in the literature⁴. The full set of EOSs contains the baseline SRO EOS, SRO_{0.75} which has $m^*/m_n = 0.75$, and its stiff variant SRO_{0.55} with $m^*/m_n = 0.55$ and soft variant SRO_{0.95} with $m^*/m_n = 0.95$ (Schneider et al. 2019a; Eggenberger Andersen et al. 2021). We also include the APR, APR_{LDP}, NRAPR, and SkAPR EOSs (Akmal & Pandharipande 1997; Akmal et al. 1998; Steiner et al. 2005; Schneider et al. 2019b); two variants of the Lattimer and Swesty (LS) EOS with incompressibilities $K_{\text{sat}} = 180$ (LS180) and $220 \text{ MeV baryon}^{-1}$ (LS220) (Lattimer & Swesty 1991; O’Connor & Ott 2011); the DD2, FSU-Gold, TM1, and TMA EOSs (Hempel et al. 2012); the IU-FSU EOS (Fattoyev et al. 2010); the two DD2 variants that include hyperons: BHB_Λ and BHB_{Λφ} (Banik et al. 2014); the H. Shen EOS (Shen et al. 1998) and its variant including Λ hyperons (Shen et al. 2011c); the SFHo and SFHx EOSs (Steiner et al. 2013); the To-

³ To handle the accuracy needed at very low densities we extend the Timmes & Arnett (1999) EOS code, `timmes.tbz` found in https://cococubed.com/code_pages/eos.shtml, to quadruple precision.

⁴ The stiff NL3 (Hempel et al. 2012) and LS375 (Lattimer & Swesty 1991; O’Connor & Ott 2011) EOSs were not considered as they would require us to rely on our neutrino emission template in regions of $M_{500} - \dot{M}_{500}$ parameter space where it becomes unreliable.

² This approach ignores that a shock-wave is created at the surface of the PNS and travels outwards before stalling and falling back onto the PNS. However, this is not relevant as this region is sonically disconnected from the outer layers by the supersonic accretion flow, where the sound pulse we are interested in forms.

gashi EOS (Togashi et al. 2017); and the Furusawa EOS (Furusawa et al. 2017).

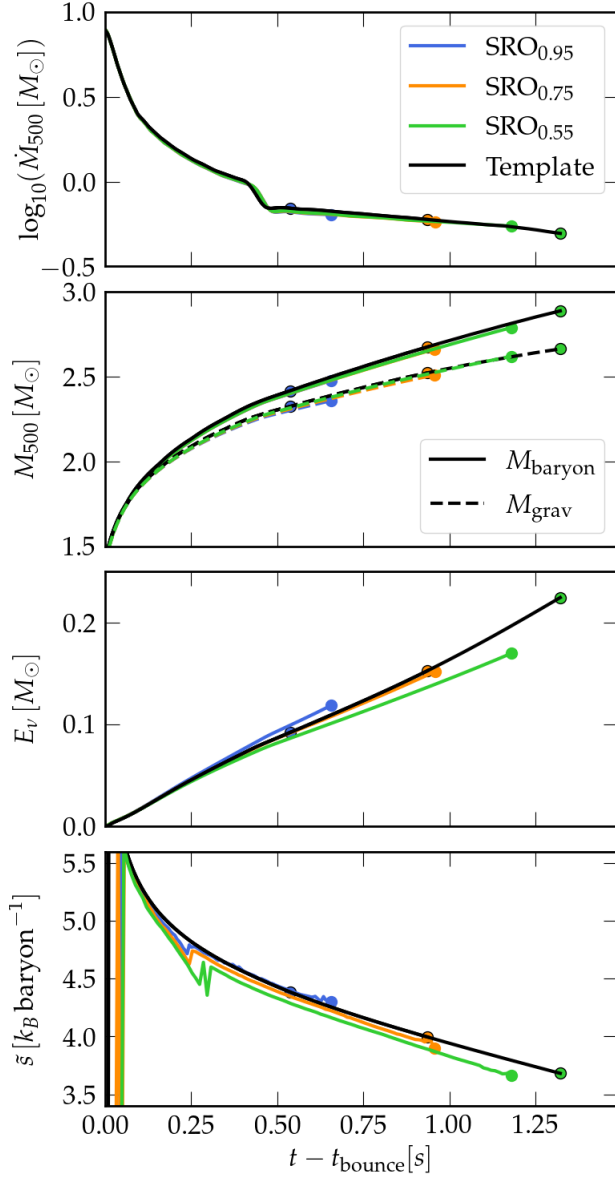


Figure 4. Comparisons of time evolution of mass accretion rate at 500 km \dot{M}_{500} (first panel), baryonic M_{baryon} and gravitational M_{grav} masses inside 500 km (second panel), the energy emitted in neutrinos E_{ν} (third panel) and entropy \tilde{s} (fourth panel) obtained using M1 neutrino transport and the parameterizations discussed in Section 2. Results are for the SRO EOSs with $m^*/m_n = 0.55, 0.75$, and 0.95 (Schneider et al. 2019b). Simulation endpoints are marked by circles. Deviations in final masses and entropy are at most a few percent, while deviations in total mass loss by neutrino emission can be up to $\sim 20\%$.

In Figure 4, we compare results of simulations that use the simplified templates, discussed in Section 2, to simulations performed using a full M1 neutrino-transport scheme for the three SRO EOS variants. We show that simulations using the simplified neutrino transport scheme predicted the evolution of the PNS entropy, the integrated neutrino luminosity E_{ν} , and the PNS gravitational mass M_{grav} within a few percent of their equivalent M1 neutrino-transport runs. However, since our template was built for a single EOS the end of the runs occur earlier (later) by up to 20% of the run time for EOSs softer (stiffer) than the baseline SRO_{0.75} EOS. This occurs because the stiffness of the EOS at a given entropy affects the neutrino luminosity: softer EOSs lead to faster PNS contraction and, therefore, faster heating and higher neutrino emission rates (Schneider et al. 2019b; Yasin et al. 2020). This effect, though, is not taken into account on our template, which is based solely on M_{500} and \dot{M}_{500} . Thus, the integrated neutrino luminosity by BH formation time predicted by our template can also differ by up to $\sim 20\%$ from the M1 neutrino-transport runs depending on progenitor and EOS used. We stress that this $\sim 20\%$ difference in BH formation time and total gravitational mass loss (integrated neutrino luminosity) is only a *secondary* source of uncertainty as the total gravitational mass loss due to neutrino emission by BH formation time can differ by a factor of ~ 2 for different EOSs for the same progenitor (S20; I21).

We extend the analysis above to the other 19 EOSs considered by comparing deviations in observables A , $\sigma_A = 1 - A^{(\text{template})}/A^{(\text{M1})}$, obtained from M1-transport simulations and their counterparts that use our parameterized model. In Figure 5, we plot the deviations between the two approaches for the BH formation time t_{BH} , gravitational mass M_{grav} , PNS gravitational mass δM_{grav} (which is equal to the total integrated neutrino luminosity E_{ν}), and PNS entropy \tilde{s} . The last 3 quantities are computed ~ 1 ms before black hole formation time t_{BH} . Although there are EOS-dependent variations in the predictions made for all of these quantities, the deviations are usually only a few percent for $\sigma_{M_{\text{grav}}}$ and $\sigma_{\tilde{s}}$. Meanwhile, BH formation time and total neutrino luminosity have relative deviations that can be up to a factor of ~ 10 larger, $\sigma_{t_{\text{BH}}} \lesssim 20\%$ ($\lesssim 100$ ms) and $\sigma_{E_{\nu}} \lesssim 25\%$.

Moreover, we note that the average neutrino emission rate, $\delta M_{\text{grav}}/t_{\text{BH}}$, is also satisfactorily approximated by our template, even if the total emitted neutrino energy by BH formation time deviates by up to 20% in some cases due to difference in predicted t_{BH} . In fact, except for EOSs that are very stiff in their temperature dependence (SRO_{0.55} EOS) or very soft (SRO_{0.95}, FSU-GOLD, LS₁₈₀, LS₂₂₀, SFHo, and Togashi EOSs), the average neutrino emission rate computed from our template is within 5% of the one obtained from M1-transport simulations. Even EOSs that are very soft

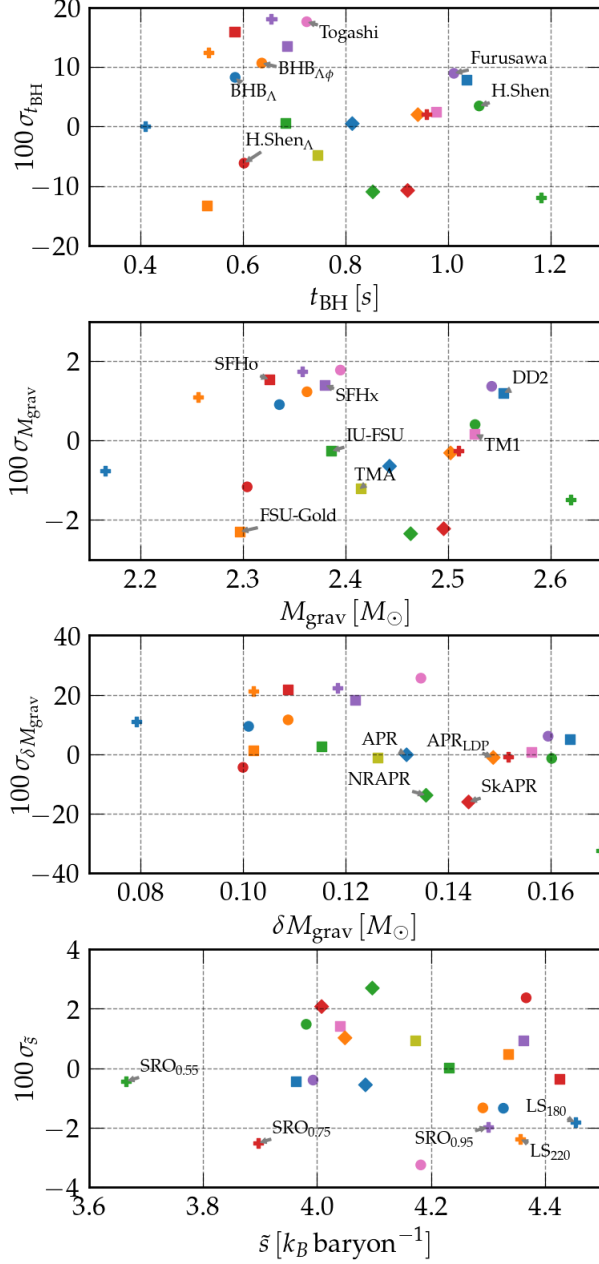


Figure 5. Deviations σ at BH formation time between core-collapse simulations for the s40WH07 progenitor of Woosley & Heger (2007) using M1 neutrino transport and the parameterized model discussed in Section 2. We plot deviations in BH formation time t_{BH} (first panel), gravitational mass inside 500 km M_{grav} (second panel), total PNS gravitational mass loss δM_{grav} (third panel), and PNS entropy ξ (fourth panel), all at t_{BH} . Plots have the full transport results in the horizontal axis and include deviations for 22 EOSs found in the literature.

or very stiff and, thus, have a larger deviation in the predicted PNS binding energy, $|\sigma_{\delta M_{\text{grav}}}| \sim 20\%$, have relative deviations in average neutrino emission rate a

factor of 2 to 4 lower, $|\delta M_{\text{grav}}|/t_{\text{BH}} \simeq 5 - 10\%$. See for example the slopes of E_{ν} for the SRO_{0.55} and SRO_{0.95} EOSs in Figure 4.

From the reasons stated above, we deem that our approximations yield acceptable results for BH formation time and gravitational mass loss from neutrino emission in CCSNe, at least for pre-SN progenitor stars that collapse into a BH within a few seconds. For PNSs that take much longer than one second to collapse into a BH we expect that our model will be even more accurate, since most of the PNS gravitational mass loss occurs when the PNS is relatively cold and, thus, when an approximately linear relationship exists between change in baryonic mass and gravitational mass or PNS binding energy. In fact, for all EOSs considered in this work $dE_{\text{bind}}/dM_{\text{baryon}} \simeq 0.30 - 0.35$.

Hence, we can use our model to study EOS effects in failed CCSNe for different progenitors without having to resort to simulations that include complex detailed and computationally expensive neutrino transport. As discussed above, this should work even for very low-compactness progenitors, which may take weeks after core bounce to accrete enough matter to collapse into a BH.

3.1. Computational Considerations

Due to the simplicity of our PNS model we are able to evolve a progenitor from core collapse until material is ejected from its surface using significantly less computational resources than are needed to evolve the same progenitor from core collapse to BH formation considering neutrino transport. Typically, each of our simulations costs between 32 and 128 CPU hours on the TETRALITH supercomputer using 8 CPU cores. This compares favorably to approximately 50 CPU hours per second of PNS evolution when using M1 neutrino-transport with FLASH as in S20. Furthermore, the computational cost is expected to be significant larger in fully relativistic simulations, such as those using GR1D as in I21. This shows that even detailed non-relativistic simulations exploring detailed neutrino transport would be unfeasible with limited resources for stars that take $\gtrsim 10$ s to collapse into BHs. However, as I21 showed, detailed simulations may not be necessary to determine mass ejecta from failed CCSNe as long as the mass loss rate and timescale in the PNS are reasonably well described. As we have argued, our approach does just that.

4. RESULTS

4.1. Pulse dynamics overview

Using the model described above we can estimate the neutrino emission from a PNS up to the point of BH formation and explore the aftermath of the BH-enveloping star. Due to neutrino emission a pressure wave appears deep within the star and propagates outwards. We now discuss the dynamics of this pulse. To facilitate direct comparisons to the work of F18, we first describe the

same progenitors plotted in their Figures 4 and 5, *i.e.*, a red supergiant (RSG) with $M_{\text{ZAMS}} = 15 M_{\odot}$ (R15z00), a blue supergiant (BSG) with $M_{\text{ZAMS}} = 25 M_{\odot}$ (B25z00), and a Wolf-Rayet (WR) star with $M_{\text{ZAMS}} = 40 M_{\odot}$ (W40z00), all with solar metallicity. EOS effects are gauged by comparing $M_{\text{grav}}^{\text{max}} = 2.0 M_{\odot}$, proxy for a soft EOS, to $M_{\text{grav}}^{\text{max}} = 2.5 M_{\odot}$, proxy for a stiff EOS. While the $2.0 M_{\odot}$ limit is likely a physical lower limit for BH formation from PNS collapse, $M_{\text{grav}}^{\text{max}} = 2.5 M_{\odot}$ should be close to the upper limit for BH formation and is the same limit set by F18.

In Figure 6, we plot stellar profiles for velocity, mach number, density, and temperature from core bounce until the simulations are stopped. Qualitatively and, to a degree, quantitatively our results agree well with those of F18. For the progenitors shown in Figure 6, a sound pulse is created deep inside the star and first acquires a positive velocity in the carbon-oxygen shell, which extend from $10^8 \text{ cm} \lesssim r \lesssim 3 \times 10^{10} \text{ cm}$. The pulse propagates outwards and speeds up or slows down according to local stellar structure, accelerating to $v^{\text{max}} \simeq 500 - 1000 \text{ km s}^{-1}$ ($v^{\text{max}} \simeq 100 - 300 \text{ km s}^{-1}$) for PNSs that collapse into a BH when the PNS mass reaches $M_{\text{grav}} = 2.5 M_{\odot}$ ($2.0 M_{\odot}$). As this occurs, pulse speed becomes comparable to local sound speed, Mach number $\text{Ma} \gtrsim 0.1$, and the pulse develops clearly defined leading and trailing edges (F18).

WR stars, here represented by the W40z00 pre-SN progenitor (right plots of Figure 6), have their carbon-oxygen core exposed as they lose both their hydrogen and helium envelopes prior to core collapse. Thus, due to the relatively small size of these stars and the sharp density gradient near the stellar surface, the pulse accelerates quickly and its speed increases $\gtrsim 10$ fold, reaching $\simeq 100 \text{ Ma}$ as it leaves the star.

Meanwhile, BSG stars (represented by the B25z00 progenitor in the center plots of Figure 6) still retain most of their helium envelopes by core collapse and the pulse approximately maintains its speed as it propagates through this layer. More generally, as a sound pulse propagates through the helium envelope of a star its mass and velocity can either increase or decrease by a factor of a few, depending on the EOS and progenitor structure, before speeding up significantly as it crosses the surface of the star and reaching speeds $\simeq 10 \text{ Ma}$.

RSG stars (represented by the R15z00 progenitor in the left plots of Figure 6), on the other hand, still maintain both their helium and hydrogen shells until core collapse. In these progenitors, the propagating pressure wave can loose up to 90% of its velocity as it crosses the outermost layers of the star before picking up speed again and crossing the stellar surface at a few Ma.

Simulations using the soft and stiff EOS proxies differ in that for stiff EOSs the pulse is both faster and more extend, indicating that it carries away more mass and energy. Besides the pulse formed deep within the star, we also note that a second pulse appears in the

stellar surface-atmosphere interface prior to the pulse arrival. These surface pulses were predicted by Coughlin et al. (2018) and also appear in the simulations of I21, although it is difficult to estimate their significance as the atmosphere thermodynamics are not fully consistent due to the lower temperature limit of our EOS tables, $T_{\text{low}} = 10^4 \text{ K}$.

4.2. Ejecta properties

In Figure 7, we plot the time evolution of pulse properties as they propagate outwards through the star for the same three progenitors discussed in Section 4.1. Here we define the pulse as the region of the star between the trailing edge, the stellar zone where velocity first becomes larger than 1% of the maximum speed, and the front edge, the furthest radial coordinate that has velocity over half of the maximum speed⁵. This is a good approximation when the shock has developed, although it underestimates the size of the pulse early on, when the front edge is not as well defined. The properties are shown for four distinct values of the maximum mass supported by PNSs at the time of BH formation: $M_{\text{grav}}^{\text{max}}/M_{\odot} = 2.0, 2.2, 2.4$, and 2.6 . The $M_{\text{grav}}^{\text{max}}$ limits were chosen based on the most physically sound EOSs available that were still close to the bounds of our neutrino emission model.

In the first row of Figure 7, we plot the evolution of internal energy E_{int} , gravitational energy E_{grav} , kinetic energy E_{kin} , and total energy E_{tot} contained in the pulse. Depending on the EOS proxy, *i.e.*, the value of $M_{\text{grav}}^{\text{max}}$, the maximum kinetic energy imparted to the pulse due to loss of core gravitational mass changes by a factor of ~ 10 to ~ 30 for a given CCSN progenitor. Although the variation in E_{kin} depends on progenitor, it is a monotonically increasing function of the PNS mass $M_{\text{grav}}^{\text{max}}$ at BH formation time. Also, the EOS dependent variations in E_{kin} lead to pronounced differences in pulse properties that persist as the pulse crosses the surface of the star and part of it becomes unbound. The choice of EOS impacts the kinetic energy of the ejecta by as much as factor of ~ 20 for the RSG and ~ 40 for the BSG and WR progenitors.

In the second row of Figure 7, we plot the evolution of the total pulse mass M_{pulse} and the total unbound mass $M_{v > v_{\text{esc}}}$. The latter quantity is obtained comparing the *local* pulse and escape velocities. We expect the true total unbound mass to be located between these two extrema as the pulse mass is increasing and the unbound mass decreasing by the end of the simulations. Simu-

⁵ We exclude the pulses that develop at the stellar surface-atmosphere interface by setting a cap on the lowest density considered as part of the pulse to be at least half of the lowest density in the pulse in the previous step. We evaluate pulses starting at 10 s after core bounce and increase the analysis time by $\sim 1 - 2\%$ every analysis step until any part of the pulse has $T < 1.01 \times 10^4 \text{ K}$ or the pulse leaves the simulation volume.

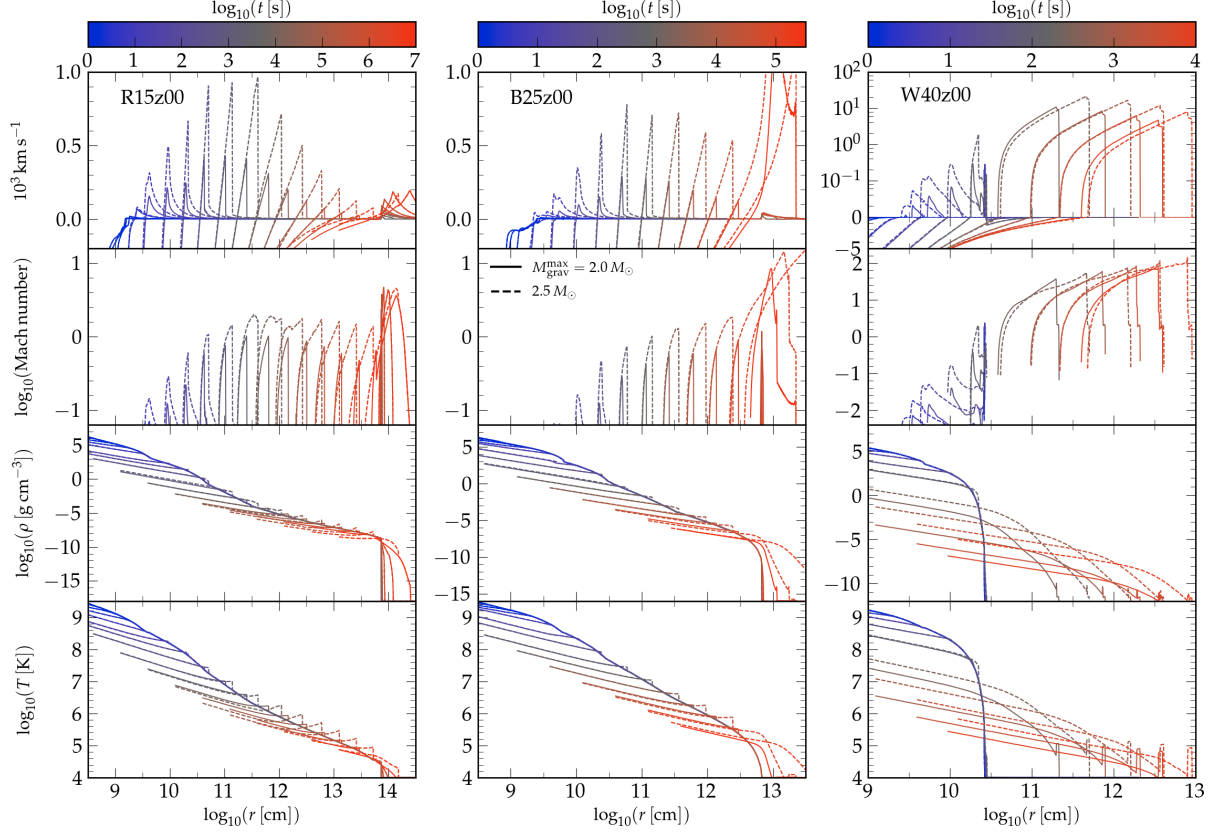


Figure 6. Pulse profiles as they propagate through the star at $t = 10^{k/2}$ s for $k \in \mathbb{N}$. We plot velocity (first row), Mach number (second row), density (third row), and temperature (fourth row) profiles for three pre SN progenitors, R15z00 (left column), B25z00 (center column), and W40z00 (right column) for two distinct maximum mass limits $M_{\text{grav}}^{\text{max}}$ supported by PNSs: $M_{\text{grav}}^{\text{max}} = 2.0 M_{\odot}$ (dashed lines) and $2.5 M_{\odot}$ (solid lines). For the W40z00 progenitor velocity profiles we change to a logarithm scale at 10 km s^{-1} .

lations that employed softer EOSs, *i.e.*, smaller $M_{\text{grav}}^{\text{max}}$, showed a larger gap between M_{pulse} and $M_{v>v_{\text{esc}}}$ at the end of the runs than simulations that used stiffer EOSs, larger $M_{\text{grav}}^{\text{max}}$. For example, M_{pulse} is as large as a factor of 10 than $M_{v>v_{\text{esc}}}$ for simulations of the R15z00 progenitor employing $M_{\text{grav}}^{\text{max}} = 2.0 M_{\odot}$, since this run ends at about the same time that the leading edge of the pulse becomes unbound. The difference is much smaller for simulations of the W40z00 progenitor since the pulse can propagate for a long time outside of the star before simulations are terminated, allowing the necessary time for M_{pulse} and $M_{v>v_{\text{esc}}}$ to converge. The unbound mass by the end of the simulation is at least $0.1 M_{\odot}$ for the R15z00 progenitor, but may be as high as $5 M_{\odot}$ when considering the stiffest EOSs in our runs. Meanwhile, a progenitor such as B25z00 (W40z00) is not likely to eject more than $0.1 M_{\odot}$ ($10^{-3} M_{\odot}$), but ejects at least $\simeq 10^{-3} M_{\odot}$ ($\simeq 10^{-6} M_{\odot}$) through the failed CCSN mechanism. Lovegrove & Woosley (2013); Fernández et al. (2018); Ivanov & Fernández (2021) pointed out that a significant uncertainty in the mass ejected and its energy is due to pre-SN progenitor structure, while I21 showed that EOS effects may lead to a factor of a

few uncertainty in the total mass ejected during a failed CCSN. However, our results show that this uncertainty may be even larger and span a few orders of magnitude for some progenitors.

Finally, we discuss the third row of Figure 7. We note that the *qualitative* behavior of the maximum velocity and the escape velocity where speed is at a maximum is the same for every progenitor, regardless of EOS. Quantitatively, however, the highest pulse velocities for each progenitor occur for EOSs that take the longest to form BHs. Since high outgoing velocities mean that the pulse travels faster throughout the star and, furthermore, the local escape velocity decreases with the distance to the center of the star, this means that the more time a BH takes to form the more mass becomes unbound and the earlier this happens. We find no cases where an increase in time to form a BH results in increased ejecta mass and lower ejecta velocity or vice versa.

In Table 2 we compare some of our predictions for ejecta properties and BH formation for the three progenitors discussed above considering $M_{\text{grav}}^{\text{max}} = 2.0$ to $2.6 M_{\odot}$ in $0.1 M_{\odot}$ steps. We also include results from the interpolation mass loss model (Model I) in Table 3 for the

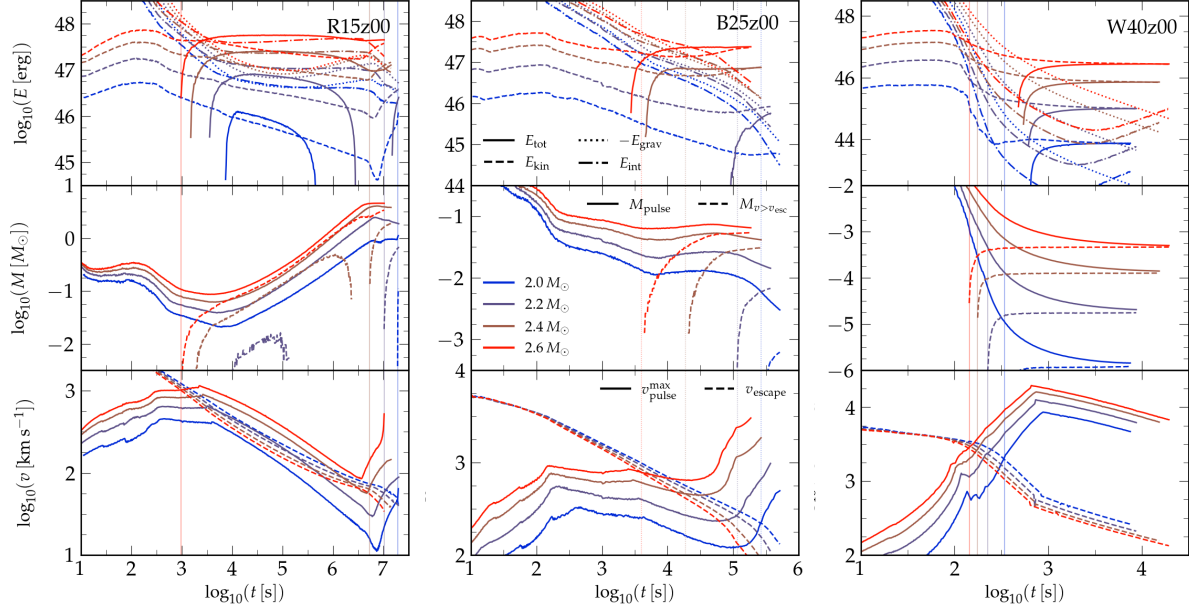


Figure 7. Pulse properties as they propagate through the star as a function of time. We plot internal E_{int} , gravitational E_{grav} , kinetic E_{kin} , and total E_{tot} energies (first row); total pulse mass M_{pulse} and unbound mass $M_{v>v_{\text{esc}}}$ (second row); and maximum pulse velocity $v_{\text{pulse}}^{\text{max}}$ and escape velocity v_{escape} where $v = v_{\text{pulse}}^{\text{max}}$. Plots are shown for 4 values of $M_{\text{grav}}^{\text{max}}$ supported by PNSs: $M_{\text{grav}}^{\text{max}} = 2.0 M_{\odot}, 2.2 M_{\odot}, 2.4 M_{\odot}$, and $2.6 M_{\odot}$. Vertical lines mark the last moment where the maximum velocity in the pulse is smaller than the escape velocity.

I21 for SFHo, LS220, and DD2 EOSs and results from the high resolution exponential mass loss model, eHR, in Table 2 of F18.

Quantitative understanding of our results in light of those of F18; I21 is difficult as we do not observe any clear trends that carry across progenitors and EOSs. For example, for the RSG progenitor R15z00 we observe that setting $M_{\text{grav}}^{\text{max}} = 2.2 M_{\odot}$ produces results similar to those of I21 using the SFHo EOSs for pulse mass M_{pulse} , BH formation time t_{BH} , and total energy emitted in neutrinos δM_{grav} . However, the total predicted pulse energy E_{tot} is much higher in our simulations: while we predict a pulse that is unbound ($E_{\text{tot}} > 0$), I21 predicts that the pulse remains bound to the star. For the BSG progenitor B25z00 the results for the SFHo EOS of I21 are similar to ours where $M_{\text{grav}}^{\text{max}} = 2.3 M_{\odot}$ for M_{pulse} , t_{BH} , δM_{grav} ; however, this time I21 predict a pulse energy E_{kin} that is almost twice that of our simulations. Finally, for the WR star progenitor W40z00 the SFHo results of I21 agree well with ours when $M_{\text{grav}}^{\text{max}} = 2.4 M_{\odot}$, except for the BH formation time t_{BH} , which is 20% longer in our run.

The trend of BHs forming with larger masses for more compact progenitors is exactly what is predicted by S20 and discussed here in Section 2.1. Nevertheless, from Figure 13 of S20, we expected that simulations employing the LS220 EOS would collapse into a BH in a slightly shorter time than those employing the SFHo EOS, which is not what was observed by I21 and shown here in Table 2. This discrepancy may be due to the

mass offset necessary to keep consistency between the inner region of the simulations of I21 performed with GR1D and the outer regions that are computed using FLASH; see their Equation 5 and Figure 2 where the mass loss due to neutrino emission for the LS220 EOS runs has a $0.02 M_{\odot}$ shift added before core bounce. Finally, our results for the RSG and BSG progenitors are comparable to the eHR model of F18, where BHs always form with a mass of $M_{\text{grav}}^{\text{max}} = 2.5 M_{\odot}$, except for the total energy carried away by neutrinos δM_{grav} (total energy of the ejecta E_{tot}) in the RSG (BSG) case. Meanwhile, for the more compact progenitor star W40z00, F18 results are more in line with our $M_{\text{grav}}^{\text{max}} = 2.6 M_{\odot}$ EOS proxy.

Besides the progenitors discussed above, we simulate failed CCSN for the other progenitors of F18, see Table 1, incrementing $M_{\text{grav}}^{\text{max}}$ from 2.0 to $2.6 M_{\odot}$. In Figure 8, we summarize our results for the distribution of total pulse kinetic energy E_{kin} and mass M_{ejecta} as well as its average velocity $\langle v_{\text{ejecta}} \rangle = \sqrt{2E_{\text{kin}}/M_{\text{ejecta}}}$, at the time the pulse reaches the atmosphere. Simulations with different $M_{\text{grav}}^{\text{max}}$ are plotted in a blue to red color-scale. We do not include results for the B80z00 progenitor because, unlike results from F18; I21, none of our simulations for this progenitor produced any unbound material. The gray symbols in the plot are results for CCSNe simulations of 262 progenitors found in the literature setting $M_{\text{grav}}^{\text{max}} = 2.5 M_{\odot}$ and will be discussed in more detail in Sections 4.3 and 4.4.

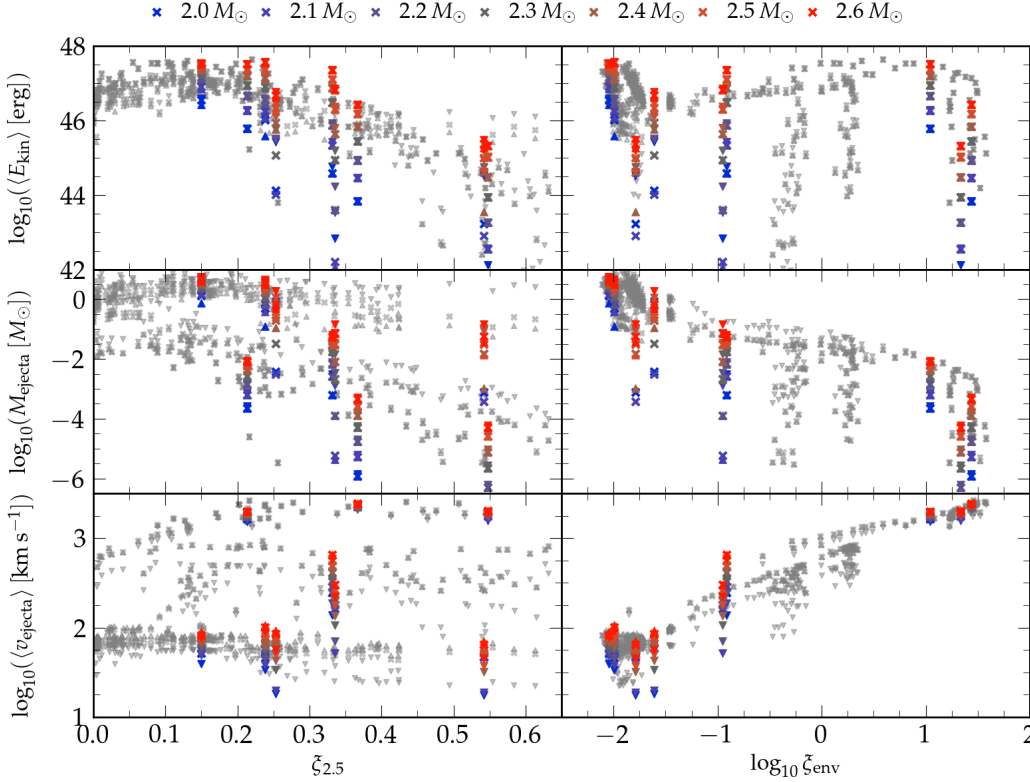


Figure 8. Estimates for ejecta kinetic energy E_{kin} (top row), mass M_{ejecta} (middle row), and average velocity $\langle v_{\text{ejecta}} \rangle$ (bottom row) for failed CCSNe simulations for progenitors with core compactness $\xi_{2.5}$ (left column) and envelope compactness ξ_{env} (right column). Results are shown for our simulations using the F18 progenitors and different mass limits for BH formation between 2.0 and $2.6 M_{\odot}$ (blue to red color scale) and for another 262 progenitors found in the literature setting $M_{\text{grav}}^{\text{max}} = 2.5 M_{\odot}$. Crosses indicate estimates of ejecta mass considering hydrogen recombination, while triangles pointing up consider unbound mass ignoring hydrogen recombination and triangles pointing down consider all matter in the pulse at the end of the simulation.

For the quantities plotted, we consider the entire pulse at the end of the run as an upper limit of possible ejected mass, while the mass of the pulse that is unbound is taken as a lower limit. We also estimate a value between these two extremes considering how much mass would be ejected if all hydrogen recombination energy were converted into kinetic energy (Lovegrove & Woosley 2013). The recombination energy is computed as in F18; I21

$$E_{\text{rec}} = \frac{\chi_H}{m_p} \int_{\text{pulse}} X_H(M) dM, \quad (3)$$

where $\chi_H = 13.6 \text{ eV}$ is the energy emitted by a hydrogen nucleus as it binds an electron, m_p is the proton mass, and the integral over the hydrogen mass fraction $X_H(M)$ is performed over the different zones that form the pulse. A key difference between how F18; I21 determine the amount of unbound mass and how we do is that we opt to compute whether any part of the pulse is locally unbound instead of determining if the entire pulse is unbound.

First we notice that for a given progenitor uncertainty in the EOS, probed by different values of $M_{\text{grav}}^{\text{max}}$, can lead to changes of a few orders of magnitude in the pre-

dicted pulse ejecta energy and mass. This is true regardless of whether we consider the whole pulse mass or only the unbound mass, and whether we include or not hydrogen recombination energy. These are much wider ranges than observed by I21 comparing the soft DD2 EOS and the stiff SFHo EOS. This result is not surprising given that for these two EOSs BHs should form with initial masses that differ by $\lesssim 0.4 M_{\odot}$, see Figure 13 in S20, a smaller range than the one we explore here. In most cases, though, much of the spread in the pulse mass M_{ejecta} and kinetic energy E_{kin} are due to simulations employing the softest EOSs, which predict a short time till BH formation and the pulses formed may not even acquire enough energy to become unbound by the time it reaches the atmosphere, even when we consider the energy input from hydrogen recombination. Nevertheless, despite large variations in predictions of pulse unbound mass and kinetic energy, the dispersion in the average ejected material velocity $\langle v_{\text{ejecta}} \rangle$, whenever some material is unbound, is significantly smaller. Note that $\langle v_{\text{ejecta}} \rangle^2 / 2 = \langle E_{\text{kin}} \rangle / M_{\text{ejecta}}$ is a measure of average energy per unit mass in both the pulse and the ejected material. This average ve-

Table 2. Comparison between pulse mass M_{pulse} , total pulse energy E_{tot} , BH formation time t_{BH} , and PNS gravitational mass loss δM_{grav} for the **R15z00**, **B25z00**, and **W40z00** progenitors from runs of Model I of [I21](#) using the SFHo, LS220 and DD2 EOSs, the high resolution model eHR of [F18](#), and our proxy EOSs with $M_{\text{grav}}^{\text{max}} = 2.0$ to $2.6 M_{\odot}$.

	M_{pulse}	E_{tot}	t_{BH}	δM_{grav}
R15z00	$[M_{\odot}]$	$[10^{47} \text{ erg}]$	$[s]$	$[M_{\odot}]$
SFHo	2.19	−0.119	2.836	0.196
LS220	2.42	−0.103	2.947	0.222
DD2	3.37	0.489	> 4.359	> 0.262
eHR	4.2	1.9	6.1	0.30
2.0	1.14	−0.024	1.679	0.120
2.1	1.38	0.041	2.356	0.157
2.2	1.89	0.204	3.146	0.200
2.3	2.72	0.689	4.061	0.250
2.4	3.84	1.05	5.099	0.304
2.5	4.39	1.88	6.281	0.361
2.6	4.58	3.31	7.652	0.425
B25z00	$[10^{-2} M_{\odot}]$	$[10^{47} \text{ erg}]$	$[s]$	$[M_{\odot}]$
SFHo	2.80	0.399	1.791	0.173
LS220	3.18	0.593	1.864	0.198
DD2	5.45	1.76	2.895	0.261
eHR	4.9	1.6	3.1	0.24
2.0	0.30	−0.005	0.880	0.087
2.1	0.77	−0.001	1.212	0.114
2.2	1.44	0.032	1.576	0.144
2.3	2.79	0.224	1.983	0.179
2.4	4.14	0.621	2.457	0.219
2.5	5.24	1.12	2.939	0.259
2.6	6.49	2.06	3.438	0.299
W40z00	$[10^{-4} M_{\odot}]$	$[10^{47} \text{ erg}]$	$[s]$	$[M_{\odot}]$
SFHo	1.44	0.067	1.535	0.157
LS220	1.63	0.077	1.570	0.184
DD2	6.30	0.326	2.466	0.242
eHR	5.0	0.25	2.6	0.22
2.0	0.014	0.001	0.501	0.060
2.1	0.062	0.003	0.806	0.086
2.2	0.200	0.008	1.14	0.115
2.3	0.572	0.027	1.50	0.147
2.4	1.40	0.068	1.89	0.184
2.5	2.86	0.146	2.32	0.221
2.6	5.00	0.267	2.77	0.260

locity and, similarly, the kinetic energy per unit mass are well correlated to envelope compactness ξ_{env} , pro-

vided that we ignore results for very soft EOSs for some of the progenitors, but mostly uncorrelated with core compactness $\xi_{2.5}$.

4.3. Effect of core compactness

We now fix the mass at BH formation to $M_{\text{grav}}^{\text{max}} = 2.5 M_{\odot}$ and discuss how progenitor properties affect the ejecta kinetic energy, mass and average velocity. To obtain a clearer picture we increase the set of progenitors studied so that we explore thoroughly the range of core and envelope compactness of pre-SN progenitors found in the literature. Thus, besides the 10 progenitors from [F18](#), we also simulate 52 progenitors from [Sukhbold et al. \(2016\)](#) with solar metallicity, 36 progenitors from [Sukhbold et al. \(2018\)](#) (12 progenitors with the standard mass loss of [Nieuwenhuijzen & de Jager \(1990\)](#), 12 with half of standard mass loss, and 12 with one tenth of standard mass loss), 126 progenitors from [Woosley et al. \(2002\)](#) (37 with solar metallicity, 59 with ultra low metallicity, and 30 with zero metallicity), 27 rotating progenitors from [Woosley & Heger \(2006\)](#) where rotation velocities were set to zero before the start of our simulations, and 22 progenitors from [Laplace et al. \(2021\)](#) (12 stars evolved isolated and 10 stars evolved in binary systems).

For this set of progenitors the ejecta kinetic energy E_{kin} depends on core compactness $\xi_{2.5}$, top left plot of Figure 8. For low-compactness cores, $\xi_{2.5} \lesssim 0.2$, the ejecta kinetic energy is in the range $10^{46} \text{ erg} \lesssim E_{\text{kin}} \lesssim 10^{47.5} \text{ erg}$. Meanwhile, as the core-compactness increases the kinetic energy of the ejected material decreases on average. Finally, for compact cores, $\xi_{2.5} \gtrsim 0.45$, the average kinetic energy is considerably lower, $10^{42} \text{ erg} \lesssim E_{\text{kin}} \lesssim 10^{46} \text{ erg}$.

The ejected mass M_{ejecta} , however, has a different behavior than the kinetic energy E_{kin} . We observe two different “bands” for the ejected mass, center left plot of Figure 8. For one set of progenitor stars $0.1 M_{\odot} \lesssim M_{\text{ejecta}} \lesssim$ a few M_{\odot} and looks independent of compactness, even for very compact progenitor cores. For another set of stars, though, $M_{\text{ejecta}} \sim 0.1 M_{\odot}$ for low-compactness cores and decreases as the compactness increases. For this second set, progenitors with compact cores, $\xi_{2.5} \gtrsim 0.5$ eject at most $\sim 10^{-3} M_{\odot}$. As we discuss below, what distinguishes the two bands is the envelope compactness, ξ_{env} .

Finally, the average speed of the material ejected, $\langle v_{\text{ejecta}} \rangle$, shows three groups, which are mostly independent of core-compactness. In fact, the groups are well separated by mass ejected. For ejecta with $M_{\text{ejecta}} \simeq 1 M_{\odot}$ the material has an average speed of order 30 to 100 km s^{-1} , regardless of compactness. Stars that eject $0.1 M_{\odot}$ or less usually eject material with 300 to 1000 km s^{-1} , again independent of progenitor compactness. A third pattern is seen for stars that eject very little mass $\lesssim 10^{-3} M_{\odot}$, as we will show in more detail below. In this case ejecta speeds exceed 2000 km s^{-1} ex-

cept for low compactness stars, $\xi_{2.5} \lesssim 0.1$, where speeds are $500 - 1000 \text{ km s}^{-1}$.

4.4. Effect of envelope compactness

Low compactness pre-SN progenitors, $\xi_{\text{env}} \lesssim 0.1$, such as RSGs and YSGs can produce a lot of ejecta, from $\sim 0.1 M_{\odot}$ up to a few M_{\odot} , although this amount can be much smaller or non-existent for certain combinations of soft EOSs and progenitors. Whenever there is ejecta, however, it travels somewhat slowly, $\langle v_{\text{ejecta}} \rangle \simeq 10$ to 100 km s^{-1} . Thus, if most BHs form with masses close to that of the maximum currently known mass of a cold-NS, $M_{\text{grav}}^{\text{max}} \simeq 2.0 - 2.2 M_{\odot}$ (Antoniadis et al. 2013; Cromartie et al. 2020), then failed SNe from RSGs probably do not lead to detectable electromagnetic signatures, as their ejecta are slow and have low energy. Nevertheless, these systems could still shine if a disk forms due to progenitor rotation and power other types of transients (Woosley & Heger 2012).

Failed CCSNe of medium-compactness pre-SN progenitors, $\xi_{\text{env}} \sim 0.1 - 1$, a range that includes BSGs, often unbind $\gtrsim 0.01$ to $0.1 M_{\odot}$ of material. Although, again, certain combinations of soft EOSs and progenitors result in lower ejecta mass or even no ejecta at all. Qualitatively similar variations to the RSG case are seen in both the energy of the ejecta and their average velocity, which usually range from $\langle v_{\text{ejecta}} \rangle \simeq 100$ to 1000 km s^{-1} .

Progenitors with very compact envelopes, such as WR stars, always eject some of their outer layers in the EOS limits we tested, albeit never more than $0.01 M_{\odot}$ according to our simulations. Furthermore, for a given progenitor the ejecta always has similar average velocity in the range $\langle v_{\text{ejecta}} \rangle \simeq 1500$ to 2500 km s^{-1} , regardless of the EOS and how much mass is ejected. If the expected ejecta velocity for this class of progenitors is indeed almost EOS independent, this would help constrain the scope of surveys similar to the one proposed by Tsuna (2021) to search for SNRs of failed CCSNe in the LMC.

In Figure 9, we couple the plots in Figure 8 for the PNSs that form BH with $M_{\text{grav}}^{\text{max}} = 2.5 M_{\odot}$ so that the trends just discussed become more obvious. We plot the kinetic energy of the ejecta, its mass, and its average speed. The results shown are always for matter that is locally unbound when accounting for the energy available due to hydrogen recombination. We first notice that some regions of the $\xi_{2.5} - \xi_{\text{env}}$ parameter space hardly contain any progenitors at all, while others have many progenitors. Specifically, the progenitors are more likely to cluster according to whether or not they retain their hydrogen ($\xi_{\text{env}} \sim -2$ and often type II SN progenitors), helium ($\xi_{\text{env}} \sim 0$ and often type Ib SN progenitors), and carbon-oxygen ($\xi_{\text{env}} \sim 1.3$ and often type Ic SN progenitors) envelopes. Envelope properties depend mostly on ZAMS mass and metallicity and, by core collapse, are mostly independent of core properties. The exception is that pre-SN progenitor stars that form

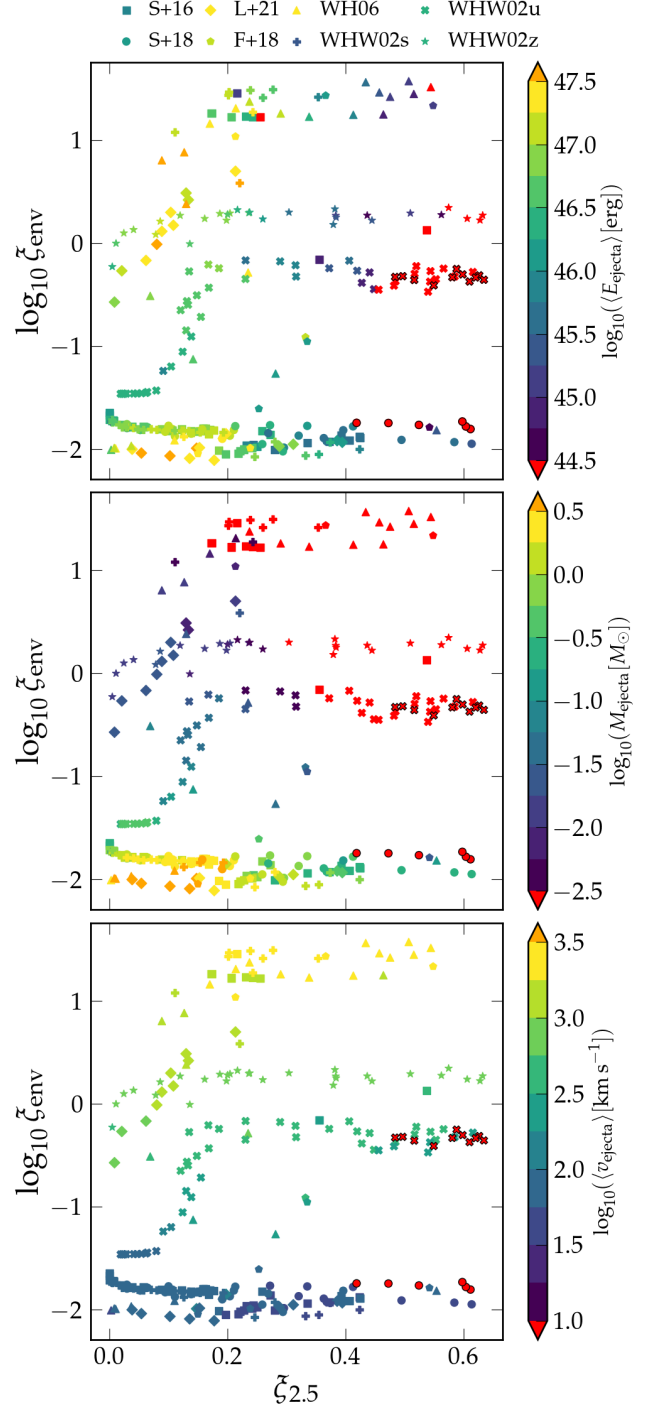


Figure 9. Kinetic energy (top), mass (center), and average velocity (bottom) of the ejecta as a function of core compactness $\xi_{2.5}$ and envelope compactness ξ_{env} for progenitors simulated setting $M_{\text{grav}}^{\text{max}} = 2.5 M_{\odot}$. S+16 are progenitors from Sukhbold et al. (2016), S+18 from Sukhbold et al. (2018), L+21 from Laplace et al. (2021), F+18 from F18, WH06 from Woosley & Heger (2006), and WHW02 from Woosley et al. (2002) with s, u, and z representing solar, ultra-low ($10^{-4} z_{\odot}$), and zero metallicity. Red symbols with black contours represent failed CCSNe that did not eject any material.

extended cores, $\xi \lesssim 0.2$, hardly ever have their carbon-oxygen envelopes exposed, $\xi_{\text{env}} \gtrsim 1$.

As discussed above, stars with extended cores and extended envelopes generally eject more mass, although this is not always the case. As a matter of fact, it is clear from Figure 9 that using only the core and envelope compactness parameters $\xi_{2.5}$ and ξ_{env} is not enough to determine the range of possible outcomes of a failed collapse event, even when considering only a single EOS proxy. For example, for $\xi_{\text{env}} \sim 0.01$ and $\xi_{2.5} \sim 0.5$ to 0.6 we find both progenitor stars that manage to eject a few $0.1 M_{\odot}$ at slow speeds as well as stars that fail to unbind any material at all. A similar statement is true for progenitors with intermediate envelope compactness, $\xi_{\text{env}} \sim 0.3$, and compact cores, $\xi_{2.5} \gtrsim 0.5$: while some progenitors do eject fast material, $\langle v_{\text{ejecta}} \rangle \simeq 1000 \text{ km s}^{-1}$, others do not produce any ejecta.

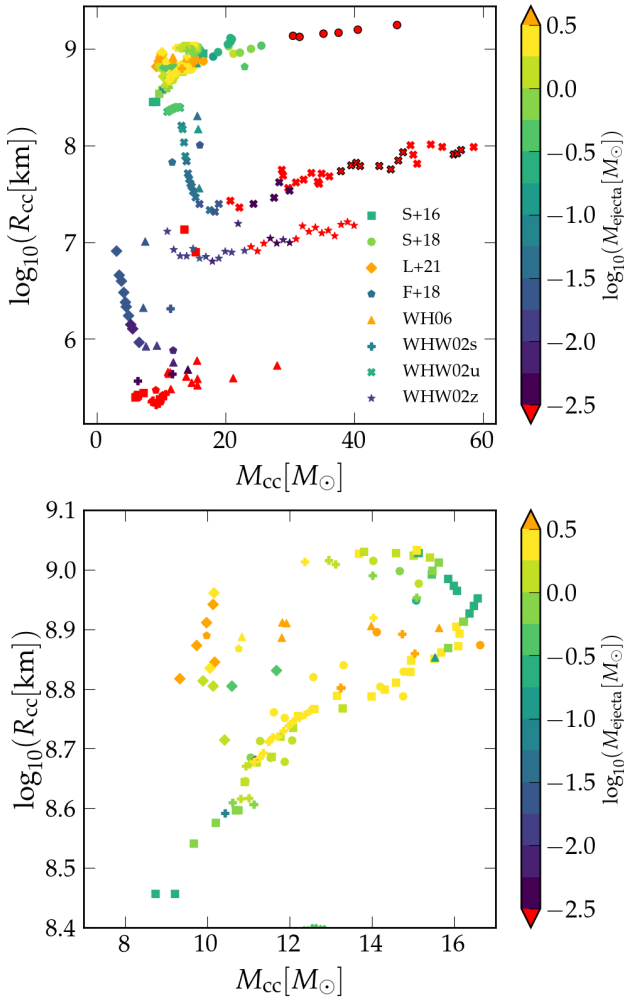


Figure 10. Ejecta mass as a function of pre-SN progenitor mass M_{cc} and radius R_{cc} at core-collapse. Bottom plot is a close-up of the low-mass large-radius region where most RSGs and YSGs cluster. Symbols are the same as in Figure 9.

In Figure 10, we show the unbound mass as a function of the progenitor mass M_{cc} and radius R_{cc} at the start of core collapse. Although these quantities are combined to determine envelope compactness ξ_{env} it is clear that they contribute separately to whether material is ejected or not. For example, we notice that progenitors that appear clustered in the region $\xi_{2.5} \gtrsim 0.5$ and $\xi_{\text{env}} \simeq 0.01$ in the plots of Figure 9 are now well separated by masses in the range from $15 M_{\odot}$ to $45 M_{\odot}$ and a large radius $R_{\text{cc}} \simeq 10^9 \text{ km}$. Finally, from this plot we also observe that progenitors that can unbind more material through the failed-SN mechanism are those that have a lower mass as their core starts to collapse and a large radius, such as RSGs and YSGs.

4.5. Effect of black hole formation time

In Figure 11 we plot the same quantities as in Figure 8, but now as a function of BH formation time t_{BH} and the total gravitational mass loss due to neutrino emission δM_{grav} .

In the top-left plot of Figure 11 we see that there is an overall scaling in the energy imparted to the pulse due to gravitational mass loss in the PNS with BH formation time that saturates if a BH takes too long to form, $t \gtrsim 10 \text{ s}$, as is the case for low core compactness progenitors. Therefore, an observational estimate of the kinetic energy of the ejecta of a failed CCSN would allow us to place some constraints on the time between the start of core collapse and BH formation. Such observation on the Milky Way or a nearby galaxy, where neutrino signals will also be measured (Sumiyoshi et al. 2006; O’Connor & Ott 2011), could be used to impose further constraints on the EOS.

In the center-left plot we show the mass of the ejecta and notice two distinct trends for the ejecta, both which saturate if collapse takes $t \gtrsim 10 \text{ s}$. This is expected since the BH formation time is approximately a function of core compactness, $t_{\text{BH}} \propto \xi_{2.5}^{-3/2}$ (O’Connor & Ott 2011) and, as we showed in Figure 8, that two trends emerged for the ejected or pulse mass as a function of the core-compactness $\xi_{2.5}$. In fact, the two trends are separated by whether or not the progenitor still has its hydrogen envelope at core-collapse, as shown in the center plot of Figure 9. Similarly, for the speed of the ejecta we observe trends that still mostly depend on envelope compactness, with little dependence on BH formation time, which depends on core compactness.

4.6. Effect of gravitational mass loss

In the top right side plot of Figure 11 we observe that, in general, ejecta kinetic energy increases with gravitational mass loss. However, the trend saturates for $\delta M_{\text{grav}} \gtrsim 0.3 M_{\odot}$ and is broken for some pre-SN progenitors. We also observe a weak correlation between ejecta mass and total gravitational mass loss, although the scatter is a few orders of magnitude. Finally, for the average ejecta speed we notice three strips that are

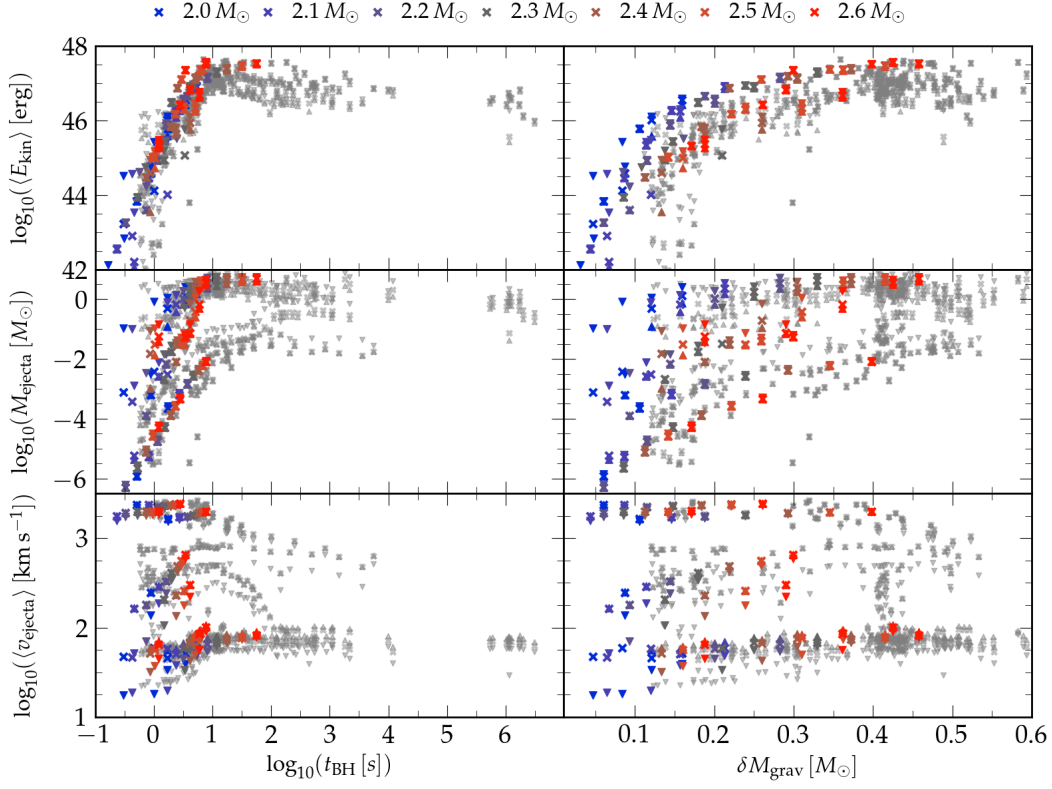


Figure 11. Same as Figure 8 but quantities are plotted as a function of BH formation time t_{BH} (left) and PNS gravitational mass loss due to neutrino emission δM_{grav} (right).

mostly uncorrelated with the PNS binding energy, each one related to the progenitor envelope properties. Thus, it is hardly possible to constrain binding energy of the PNS at the time of collapse from measurements of the velocity of the ejecta alone.

4.7. Mass ejected in the Hertzsprung–Russell diagram

When observing a distant star we can measure neither its mass nor its radius directly. Instead, we have to rely on stellar evolution codes to infer those observables from the surface temperature and luminosity of the star. Here, we approximate the pre-SN stellar luminosity using the fit of [Sukhbold et al. \(2018\)](#)

$$L_{\text{pre}} \simeq 5.77 \times 10^{38} \left(\frac{M_{\text{He}}}{6M_{\odot}} \right)^{3/2} \text{ erg s}^{-1} \quad (4)$$

where M_{He} is the mass bound by the Helium core. For stars that have lost their helium shell we use the carbon-oxygen core mass M_{CO} . The effective surface temperature T_{eff} is estimated from the luminosity L_{pre} and the pre-SN progenitor radius R_{cc} . For pre-SN progenitors that have their luminosity and surface temperatures available, such as those of [F18](#) and [Laplace et al. \(2021\)](#), we obtain deviations in the 10% range using this approximation and opt to use it for all other stars. A few exceptions do occur, but deviations are at most a factor of two from the approximation of Equation (4).

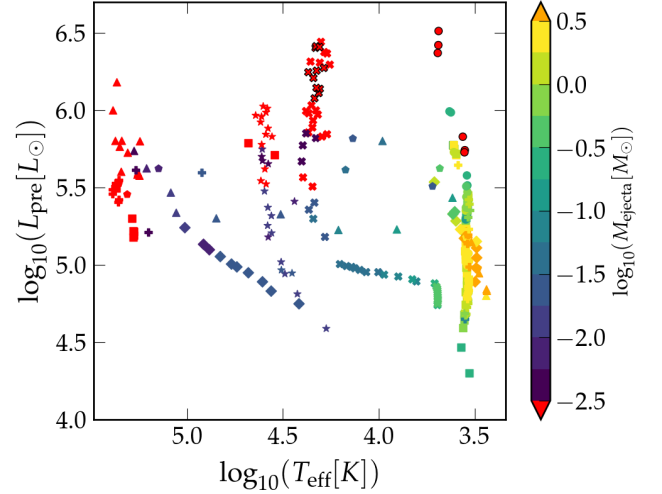


Figure 12. Ejecta mass as a function of pre-SN progenitor luminosity L_{pre} and effective surface temperature T_{eff} at the start of core-collapse. Symbols are the same as in Figure 9. Black border denote progenitors that did not eject any mass.

Using the approximations above, we plot the ejected mass as a function of the observable quantities L_{pre} and T_{eff} in Figure 12. The diagram shows that the hottest progenitors at core collapse, $T_{\text{eff}} \gtrsim 10^{4.2} \text{ K}$ usually collapse into a BH without a significant transient as they

eject little to no mass, $M_{\text{ejecta}} \lesssim 0.1 M_{\odot}$. These progenitors are often the evolutionary endpoints of massive stars with low or zero metallicity (Woosley et al. 2002), stars in binary systems (Laplace et al. 2021), or fast rotating stars that mix their shells while in the main sequence (Woosley & Heger 2006). Recall that we removed the angular momentum to simulate the latter. Because these progenitors have lost their hydrogen shells by core collapse time, in the case of a successful SN explosion they are observed as type Ib or type Ic SNe, stars that have their strongly bound helium or carbon-oxygen cores exposed, respectively.

Stars on the cold end of the diagram, RSGs or YSGs and $T_{\text{eff}} \lesssim 10^{3.7}$ K, are more likely to unbind their outer layers in the case of a failed SN. This is expected, as the hydrogen envelope these colder stars retain until their core starts to collapse are loosely bound. When these stars explode successfully, they are observed as type II SNe due to their hydrogen rich ejecta. Progenitors with luminosity $L \lesssim 10^{5.1} L_{\odot}$ have been associated with type II SN while, to date more luminous RSGs and YSGs have not (Rodríguez 2022). Thus, these stars are reasonable candidates to be progenitors of failed SNe.

5. SUMMARY & CONCLUSIONS

We developed simple templates to model the entropy evolution and neutrino emission rates of PNSs formed in CCSNe. The templates were built based on FLASH simulations that used M1 neutrino transport for 25 selected progenitors using the baseline SRO EOS of S20. Simulations using our templates reproduce the BH formation time and the PNS binding energy at BH formation time with a relative error $\lesssim 20\%$ for an intermediate compactness progenitor and different hadronic EOSs. The template also reproduces the PNS gravitational mass and entropy as well as the average neutrino emission rate of PNSs within a few percent.

Once built, the templates allow us to carry out the evolution of massive stars that undergo failed core collapse, *i.e.*, a supernova where the shock is not revived, beyond the moment a PNS becomes a BH and until material is ejected from the surface of the star. The ejecta results from the disturbance in the hydrodynamic equilibrium in the outer layers of the star due to PNS gravitational mass loss by neutrino emission (Nadyozhin 1980; Lovegrove & Woosley 2013). Due to the simplicity of the emission model we can simulate core collapse events where the PNS takes less than a second to up to weeks to accrete enough material to collapse into a BH.

With this in mind we explored how the EOS can affect failed CCSNe ejecta for different progenitor stars. In our model, EOS effects are gauged by setting the BH formation at different PNS masses. Despite the many simplifications in the core-collapse physics, our results expand upon previous works. The most significant improvement being the inclusion of a wide range of pre-SN

progenitor stars with different ZAMS masses and core and envelope compactness.

As I21, we also observe that EOS stiffness can significantly alter the total amount of mass ejected and its average energy, sometimes by a few orders of magnitude. However, the average energy per unit mass, probed by the average ejecta speed, is often not considerably affected by changes in EOS. This is especially true for stars with compact envelopes, such as WR stars, where only a small fraction of the envelope, $M_{\text{ejecta}} \ll 10^{-1} M_{\odot}$, is ejected with speeds in excess of 1000 km s^{-1} . Direct comparison of our results to those of F18; I21 show that changes in how the collapse is modeled can modify the predicted properties of the ejected mass in a failed core collapse in ways that are difficult to predict. Nevertheless, the overall qualitative picture is always the same, stiffer EOSs predict longer times to form BHs which in turn results in higher neutrino emissions and, thus, larger ejecta mass with higher average kinetic energy.

Our results also show that, even when considering that all PNSs form BHs with the same gravitational mass, core and envelope compactness, $\xi_{2.5}$ and ξ_{env} , respectively, are not enough parameters to predict the ejecta properties of a failed CCNS. Although these two parameters do allow us to make educated guesses of the ejecta mass and energy for most stars, in some cases it is also necessary to consider the total mass of the star and/or its radius at the moment of core collapse separately.

An assumption made in this work and facilitated by the fact that we only perform spherically symmetric CCSNe simulations, where the SN shock is rarely revived, was that every progenitor could collapse into a BH. However, successful SNe are routinely observed and the pre-SN progenitor envelope properties can be inferred from the emission lines from the SN explosion. Sometimes, even the pre-SN progenitors themselves are identified by direct comparison of SN images to previous observations of the same region of the sky. In fact, pre-SN progenitors that retain their hydrogen envelopes evolve into RSGs and YSGs and have been reported to explode as type II SNe (Smartt et al. 2009; Williams et al. 2014; Rodríguez 2022). At core-collapse time, these stars have an effective surface temperature $\log_{10}(T_{\text{eff}} [\text{K}]) \simeq 3.6$ and, although their luminosity spans the range $\log_{10}(L_{\text{pre}}/L_{\odot}) \simeq 4.5 - 6.5$ dex, to date only progenitors with $\log_{10}(L_{\text{pre}}/L_{\odot}) \lesssim 5.1$ dex have been directly associated to successful SN explosions (Rodríguez 2022). Thus, many of the stars in our dataset, particularly those with $\log_{10}(T_{\text{eff}} [\text{K}]) \simeq 3.6$ and $\log_{10}(L_{\text{pre}}/L_{\odot}) \gtrsim 5.1$ dex, as seen in Figure 12, could be progenitors of failed SNe as currently suggested by observations. On the other hand, spherically symmetric simulations by Boccioli et al. (2022b) employing neutrino-driven turbulent convection using time-dependent mixing length theory model (Couch et al. 2020; Boccioli et al. 2022a), suggest that some low-mass low-compactness progenitors, $M_{\text{ZAMS}} \lesssim 15 M_{\odot}$

and $\xi_{2.5} \lesssim 0.25$ and which we find to have luminosity $L \lesssim 10^5 L_{\odot}$, could also lead to failed CCSNe.

Another limitation of our work is that we did not include rotation. Angular momentum effects are very important when simulating CCSNe (O’Connor & Ott 2011; Dessart et al. 2012; Richers et al. 2017) and may lead to the development of accretion disks around the PNS which may facilitate mass ejection (Feng et al. 2018; Batta & Ramirez-Ruiz 2019; Murguia-Berthier et al. 2020). Thus, with respect to rotation, our results could be taken as lower limits to the amount of mass ejected and energy for a particular combination of progenitor and EOS. Our model could be extended to add rotation, however, this would result in an added dimension to the PNS physics and its evolution and neutrino emission templates would have to be updated accordingly.

From a practical perspective, one could compare our results to those of a failed CCSNe from a slowly or non-rotating progenitor. Then, if a failed CCSN were observed, its progenitor identified, and total ejected mass and velocity estimated, one could, in principle, validate stellar evolution models as well as place limits on the EOS of hot-dense matter and PNS properties at BH formation time based on the trends observed in the results presented here. Ideally, this would be done using a more complete picture of failed core collapse; one built from a set of simulations including more progenitors, other EOS templates validated by multi-dimensional simulations, other EOS proxies, and including rotation.

ACKNOWLEDGMENTS

The authors would like to thank S. Couch for code development within FLASH and early discussions related this work. We would also like to thank R. Fernández, for his help on how to set up the stellar surface atmosphere interface, and E. Laplace and D. Vartanyan for help with the progenitor stars from their work. We are also grateful to A. Betranhandy, S. Zha, O. Eggenberger Andersen, and H. Andresen, for fruitful discussions during development and writing of this manuscript. The authors acknowledge support from the Swedish Research Council project No. 2020-00452. The simulations were performed on resources provided by the Swedish National Infrastructure for Computing (SNIC) at PDC and NSC. Partially funded by the Swedish Research Council through grant agreement No. 2018-05973 The software used in this work was in part developed by the DOE NNSA-ASC OASCR Flash Center at the University of Chicago.

Software: FLASH (Fryxell et al. 2000; Dubey et al. 2009; Couch 2013; O’Connor & Couch 2018), NuLib (O’Connor 2015), SROEOS (Schneider et al. 2017), Timmes EOS (Timmes & Arnett 1999), Matplotlib (Hunter 2007), NumPy (Harris et al. 2020), SciPy (Virtanen et al. 2020), MESA (Paxton et al. 2011, 2013, 2015, 2018, 2019), VisIt (Childs et al. 2012).

REFERENCES

- Adams, S. M., Kochanek, C. S., Gerke, J. R., Stanek, K. Z., & Dai, X. 2017, Monthly Notices of the Royal Astronomical Society, 468, 4968, doi: [10.1093/mnras/stx816](https://doi.org/10.1093/mnras/stx816)
- Akmal, A., & Pandharipande, V. R. 1997, Physical Review C, 56, 2261, doi: [10.1103/PhysRevC.56.2261](https://doi.org/10.1103/PhysRevC.56.2261)
- Akmal, A., Pandharipande, V. R., & Ravenhall, D. G. 1998, Physical Review C, 58, 1804, doi: [10.1103/PhysRevC.58.1804](https://doi.org/10.1103/PhysRevC.58.1804)
- Allan, A. P., Groh, J. H., Mehner, A., et al. 2020, Monthly Notices of the Royal Astronomical Society, 496, 1902, doi: [10.1093/mnras/staa1629](https://doi.org/10.1093/mnras/staa1629)
- Antoniadis, J., Freire, P. C. C., Wex, N., et al. 2013, Science, 340, 1233232, doi: [10.1126/science.1233232](https://doi.org/10.1126/science.1233232)
- Banik, S., Hempel, M., & Bandyopadhyay, D. 2014, The Astrophysical Journal Supplement Series, 214, 22, doi: [10.1088/0067-0049/214/2/22](https://doi.org/10.1088/0067-0049/214/2/22)
- Basinger, C. M., Kochanek, C. S., Adams, S. M., Dai, X., & Stanek, K. Z. 2021, Monthly Notices of the Royal Astronomical Society, 508, 1156, doi: [10.1093/mnras/stab2620](https://doi.org/10.1093/mnras/stab2620)
- Batta, A., & Ramirez-Ruiz, E. 2019, Accretion Feedback from Newly-Formed Black Holes and Its Implications for LIGO Sources, arXiv. <https://arxiv.org/abs/1904.04835>
- Bear, E., Soker, N., & Kashi, A. 2022, doi: [10.48550/ARXIV.2202.08629](https://doi.org/10.48550/ARXIV.2202.08629)
- Boccioli, L., Mathews, G. J., Suh, I.-S., & O’Connor, E. P. 2022a, The Astrophysical Journal, 926, 147, doi: [10.3847/1538-4357/ac4603](https://doi.org/10.3847/1538-4357/ac4603)
- Boccioli, L., Roberti, L., Limongi, M., Mathews, G. J., & Chieffi, A. 2022b, Explosion Mechanism of Core-Collapse Supernovae: Role of the Si/O Interface, arXiv. <https://arxiv.org/abs/2207.08361>
- Burke, C. J., Baldassare, V. F., Liu, X., et al. 2020, The Astrophysical Journal, 894, L5, doi: [10.3847/2041-8213/ab88de](https://doi.org/10.3847/2041-8213/ab88de)
- Burrows, A., Radice, D., Vartanyan, D., et al. 2020, Monthly Notices of the Royal Astronomical Society, 491, 2715, doi: [10.1093/mnras/stz3223](https://doi.org/10.1093/mnras/stz3223)
- Byrne, R. A., & Fraser, M. 2022, Monthly Notices of the Royal Astronomical Society, 514, 1188, doi: [10.1093/mnras/stac1308](https://doi.org/10.1093/mnras/stac1308)

- Childs, H., Brugger, E., Whitlock, B., et al. 2012, in High Performance Visualization—Enabling Extreme-Scale Scientific Insight, 357–372, doi: [10.1201/b12985](https://doi.org/10.1201/b12985)
- Couch, S. M. 2013, *The Astrophysical Journal*, 765, 29, doi: [10.1088/0004-637X/765/1/29](https://doi.org/10.1088/0004-637X/765/1/29)
- Couch, S. M., Warren, M. L., & O'Connor, E. P. 2020, *The Astrophysical Journal*, 890, 127, doi: [10.3847/1538-4357/ab609e](https://doi.org/10.3847/1538-4357/ab609e)
- Coughlin, E. R., Quataert, E., Fernández, R., & Kasen, D. 2018, *Monthly Notices of the Royal Astronomical Society*, 477, 1225, doi: [10.1093/mnras/sty667](https://doi.org/10.1093/mnras/sty667)
- Cromartie, H. T., Fonseca, E., Ransom, S. M., et al. 2020, *Nature Astronomy*, 4, 72, doi: [10.1038/s41550-019-0880-2](https://doi.org/10.1038/s41550-019-0880-2)
- Dessart, L., O'Connor, E., & Ott, C. D. 2012, *The Astrophysical Journal*, 754, 76, doi: [10.1088/0004-637X/754/1/76](https://doi.org/10.1088/0004-637X/754/1/76)
- Dubey, A., Antypas, K., Ganapathy, M. K., et al. 2009, *Parallel Computing*, 35, 512, doi: [10.1016/j.parco.2009.08.001](https://doi.org/10.1016/j.parco.2009.08.001)
- Eggenberger Andersen, O., Zha, S., da Silva Schneider, A., et al. 2021, *The Astrophysical Journal*, 923, 201, doi: [10.3847/1538-4357/ac294c](https://doi.org/10.3847/1538-4357/ac294c)
- Fattouev, F. J., Horowitz, C. J., Piekarewicz, J., & Shen, G. 2010, *Physical Review C*, 82, 055803, doi: [10.1103/PhysRevC.82.055803](https://doi.org/10.1103/PhysRevC.82.055803)
- Feng, E.-H., Shen, R.-F., & Lin, W.-P. 2018, *The Astrophysical Journal*, 867, 130, doi: [10.3847/1538-4357/aae385](https://doi.org/10.3847/1538-4357/aae385)
- Fernández, R., Quataert, E., Kashiyama, K., & Coughlin, E. R. 2018, *Monthly Notices of the Royal Astronomical Society*, 476, 2366, doi: [10.1093/mnras/sty306](https://doi.org/10.1093/mnras/sty306)
- Fryxell, B., Olson, K., Ricker, P., et al. 2000, *The Astrophysical Journal Supplement Series*, 131, 273, doi: [10.1086/317361](https://doi.org/10.1086/317361)
- Furusawa, S., Togashi, H., Nagakura, H., et al. 2017, *Journal of Physics G: Nuclear and Particle Physics*, 44, 094001, doi: [10.1088/1361-6471/aa7f35](https://doi.org/10.1088/1361-6471/aa7f35)
- Gerke, J. R., Kochanek, C. S., & Stanek, K. Z. 2015, *Monthly Notices of the Royal Astronomical Society*, 450, 3289, doi: [10.1093/mnras/stv776](https://doi.org/10.1093/mnras/stv776)
- Harris, C. R., Millman, K. J., van der Walt, S. J., et al. 2020, *Nature*, 585, 357, doi: [10.1038/s41586-020-2649-2](https://doi.org/10.1038/s41586-020-2649-2)
- Hempel, M., Fischer, T., Schaffner-Bielich, J., & Liebendörfer, M. 2012, *The Astrophysical Journal*, 748, 70, doi: [10.1088/0004-637X/748/1/70](https://doi.org/10.1088/0004-637X/748/1/70)
- Humphreys, R. M. 2019, *Research Notes of the AAS*, 3, 164, doi: [10.3847/2515-5172/ab5191](https://doi.org/10.3847/2515-5172/ab5191)
- Hunter, J. D. 2007, *Computing in Science & Engineering*, 9, 90, doi: [10.1109/MCSE.2007.55](https://doi.org/10.1109/MCSE.2007.55)
- Ivanov, M., & Fernández, R. 2021, *The Astrophysical Journal*, 911, 6, doi: [10.3847/1538-4357/abe59e](https://doi.org/10.3847/1538-4357/abe59e)
- Kochanek, C. S., Beacom, J. F., Kistler, M. D., et al. 2008, *The Astrophysical Journal*, 684, 1336, doi: [10.1086/590053](https://doi.org/10.1086/590053)
- Laplace, E., Justham, S., Renzo, M., et al. 2021, *Astronomy & Astrophysics*, 656, A58, doi: [10.1051/0004-6361/202140506](https://doi.org/10.1051/0004-6361/202140506)
- Lattimer, J. M., & Swesty, F. D. 1991, *Nuclear Physics A*, 535, 331, doi: [10.1016/0375-9474\(91\)90452-C](https://doi.org/10.1016/0375-9474(91)90452-C)
- Limongi, M., & Chieffi, A. 2006, *The Astrophysical Journal*, 647, 483, doi: [10.1086/505164](https://doi.org/10.1086/505164)
- Lovegrove, E., & Woosley, S. E. 2013, *The Astrophysical Journal*, 769, 109, doi: [10.1088/0004-637X/769/2/109](https://doi.org/10.1088/0004-637X/769/2/109)
- Lovegrove, E., Woosley, S. E., & Zhang, W. 2017, *The Astrophysical Journal*, 845, 103, doi: [10.3847/1538-4357/aa7b7d](https://doi.org/10.3847/1538-4357/aa7b7d)
- Murguia-Berthier, A., Batta, A., Janiuk, A., et al. 2020, *The Astrophysical Journal Letters*, 901, L24, doi: [10.3847/2041-8213/abb818](https://doi.org/10.3847/2041-8213/abb818)
- Murphy, J. W., Khan, R., Williams, B., et al. 2018, *The Astrophysical Journal*, 860, 117, doi: [10.3847/1538-4357/aac2be](https://doi.org/10.3847/1538-4357/aac2be)
- Nadyozhin, D. K. 1980, *Astrophysics and Space Science*, 69, 115, doi: [10.1007/BF00638971](https://doi.org/10.1007/BF00638971)
- Neustadt, J. M. M., Kochanek, C. S., Stanek, K. Z., et al. 2021, *Monthly Notices of the Royal Astronomical Society*, 508, 516, doi: [10.1093/mnras/stab2605](https://doi.org/10.1093/mnras/stab2605)
- Nieuwenhuijzen, H., & de Jager, C. 1990, *Astronomy and Astrophysics*, 231, 134
- O'Connor, E. 2015, *The Astrophysical Journal Supplement Series*, 219, 24, doi: [10.1088/0067-0049/219/2/24](https://doi.org/10.1088/0067-0049/219/2/24)
- O'Connor, E., & Ott, C. D. 2011, *The Astrophysical Journal*, 730, 70, doi: [10.1088/0004-637X/730/2/70](https://doi.org/10.1088/0004-637X/730/2/70)
- O'Connor, E. P., & Couch, S. M. 2018, *The Astrophysical Journal*, 865, 81, doi: [10.3847/1538-4357/aadcf7](https://doi.org/10.3847/1538-4357/aadcf7)
- Paxton, B., Bildsten, L., Dotter, A., et al. 2011, *The Astrophysical Journal Supplement Series*, 192, 3, doi: [10.1088/0067-0049/192/1/3](https://doi.org/10.1088/0067-0049/192/1/3)
- Paxton, B., Cantiello, M., Arras, P., et al. 2013, *The Astrophysical Journal Supplement Series*, 208, 4, doi: [10.1088/0067-0049/208/1/4](https://doi.org/10.1088/0067-0049/208/1/4)
- Paxton, B., Marchant, P., Schwab, J., et al. 2015, *The Astrophysical Journal Supplement Series*, 220, 15, doi: [10.1088/0067-0049/220/1/15](https://doi.org/10.1088/0067-0049/220/1/15)
- Paxton, B., Schwab, J., Bauer, E. B., et al. 2018, *The Astrophysical Journal Supplement Series*, 234, 34, doi: [10.3847/1538-4365/aaa5a8](https://doi.org/10.3847/1538-4365/aaa5a8)

- Paxton, B., Smolec, R., Schwab, J., et al. 2019, The Astrophysical Journal Supplement Series, 243, 10, doi: [10.3847/1538-4365/ab2241](https://doi.org/10.3847/1538-4365/ab2241)
- Piro, A. L. 2013, The Astrophysical Journal, 768, L14, doi: [10.1088/2041-8205/768/1/L14](https://doi.org/10.1088/2041-8205/768/1/L14)
- Richers, S., Ott, C. D., Abdikamalov, E., O'Connor, E., & Sullivan, C. 2017, Physical Review D, 95, 063019, doi: [10.1103/PhysRevD.95.063019](https://doi.org/10.1103/PhysRevD.95.063019)
- Rodríguez, Ó. 2022, Monthly Notices of the Royal Astronomical Society, stac1831, doi: [10.1093/mnras/stac1831](https://doi.org/10.1093/mnras/stac1831)
- Schneider, A. d. S., O'Connor, E., Granqvist, E., Betranhandy, A., & Couch, S. M. 2020, The Astrophysical Journal, 894, 4, doi: [10.3847/1538-4357/ab8308](https://doi.org/10.3847/1538-4357/ab8308)
- Schneider, A. S., Constantinou, C., Muccioli, B., & Prakash, M. 2019a, Physical Review C, 100, 025803, doi: [10.1103/PhysRevC.100.025803](https://doi.org/10.1103/PhysRevC.100.025803)
- Schneider, A. S., Roberts, L. F., & Ott, C. D. 2017, Physical Review C, 96, 065802, doi: [10.1103/PhysRevC.96.065802](https://doi.org/10.1103/PhysRevC.96.065802)
- Schneider, A. S., Roberts, L. F., Ott, C. D., & O'Connor, E. 2019b, Physical Review C, 100, 055802, doi: [10.1103/PhysRevC.100.055802](https://doi.org/10.1103/PhysRevC.100.055802)
- Shen, G., Horowitz, C. J., & O'Connor, E. 2011a, Physical Review C, 83, 065808, doi: [10.1103/PhysRevC.83.065808](https://doi.org/10.1103/PhysRevC.83.065808)
- Shen, G., Horowitz, C. J., & Teige, S. 2011b, Physical Review C, 83, 035802, doi: [10.1103/PhysRevC.83.035802](https://doi.org/10.1103/PhysRevC.83.035802)
- Shen, H., Toki, H., Oyamatsu, K., & Sumiyoshi, K. 1998, Nuclear Physics A, 637, 435, doi: [10.1016/S0375-9474\(98\)00236-X](https://doi.org/10.1016/S0375-9474(98)00236-X)
- . 2011c, The Astrophysical Journal Supplement Series, 197, 20, doi: [10.1088/0067-0049/197/2/20](https://doi.org/10.1088/0067-0049/197/2/20)
- Smartt, S. J., Eldridge, J. J., Crockett, R. M., & Maund, J. R. 2009, Monthly Notices of the Royal Astronomical Society, 395, 1409, doi: [10.1111/j.1365-2966.2009.14506.x](https://doi.org/10.1111/j.1365-2966.2009.14506.x)
- Steiner, A., Prakash, M., Lattimer, J., & Ellis, P. 2005, Physics Reports, 411, 325, doi: [10.1016/j.physrep.2005.02.004](https://doi.org/10.1016/j.physrep.2005.02.004)
- Steiner, A. W., Hempel, M., & Fischer, T. 2013, The Astrophysical Journal, 774, 17, doi: [10.1088/0004-637X/774/1/17](https://doi.org/10.1088/0004-637X/774/1/17)
- Sukhbold, T., Ertl, T., Woosley, S. E., Brown, J. M., & Janka, H.-T. 2016, The Astrophysical Journal, 821, 38, doi: [10.3847/0004-637X/821/1/38](https://doi.org/10.3847/0004-637X/821/1/38)
- Sukhbold, T., Woosley, S. E., & Heger, A. 2018, The Astrophysical Journal, 860, 93, doi: [10.3847/1538-4357/aac2da](https://doi.org/10.3847/1538-4357/aac2da)
- Sumiyoshi, K., Yamada, S., Suzuki, H., & Chiba, S. 2006, Physical Review Letters, 97, 091101, doi: [10.1103/PhysRevLett.97.091101](https://doi.org/10.1103/PhysRevLett.97.091101)
- Timmes, F. X., & Arnett, D. 1999, The Astrophysical Journal Supplement Series, 125, 277, doi: [10.1086/313271](https://doi.org/10.1086/313271)
- Timmes, F. X., & Swesty, F. D. 2000, The Astrophysical Journal Supplement Series, 126, 501, doi: [10.1086/313304](https://doi.org/10.1086/313304)
- Togashi, H., Nakazato, K., Takehara, Y., et al. 2017, Nuclear Physics A, 961, 78, doi: [10.1016/j.nuclphysa.2017.02.010](https://doi.org/10.1016/j.nuclphysa.2017.02.010)
- Tsuna, D. 2021, Publications of the Astronomical Society of Japan, 73, L6, doi: [10.1093/pasj/psab041](https://doi.org/10.1093/pasj/psab041)
- Virtanen, P., Gommers, R., Oliphant, T. E., et al. 2020, Nature Methods, 17, 261, doi: [10.1038/s41592-019-0686-2](https://doi.org/10.1038/s41592-019-0686-2)
- Williams, B. F., Peterson, S., Murphy, J., et al. 2014, The Astrophysical Journal, 791, 105, doi: [10.1088/0004-637X/791/2/105](https://doi.org/10.1088/0004-637X/791/2/105)
- Woosley, S., & Heger, A. 2007, Physics Reports, 442, 269, doi: [10.1016/j.physrep.2007.02.009](https://doi.org/10.1016/j.physrep.2007.02.009)
- Woosley, S. E., & Heger, A. 2006, The Astrophysical Journal, 637, 914, doi: [10.1086/498500](https://doi.org/10.1086/498500)
- . 2012, The Astrophysical Journal, 752, 32, doi: [10.1088/0004-637X/752/1/32](https://doi.org/10.1088/0004-637X/752/1/32)
- Woosley, S. E., Heger, A., & Weaver, T. A. 2002, Reviews of Modern Physics, 74, 1015, doi: [10.1103/RevModPhys.74.1015](https://doi.org/10.1103/RevModPhys.74.1015)
- Yasin, H., Schäfer, S., Arcones, A., & Schwenk, A. 2020, Physical Review Letters, 124, 092701, doi: [10.1103/PhysRevLett.124.092701](https://doi.org/10.1103/PhysRevLett.124.092701)